The Astrophysical Journal, 743:47 (19pp), 2011 December 10 doi:10.1088/0004-637X/743/1/47

DIFFUSIVE PARTICLE ACCELERATION IN SHOCKED, VISCOUS ACCRETION DISKS: GREEN'S FUNCTION ENERGY DISTRIBUTION

Peter A. Becker[1], Santabrata Das[2], and Truong Le[3]
[1] School of Physics, Astronomy, & Computational Science, George Mason University, Fairfax, VA 22030-4444, USA; pbecker@gmu.edu
[2] Indian Institute of Technology Guwahati, Guwahati 781 039, Assam, India; sbdas@iitg.ernet.in
[3] The Governor's School for Science and Technology, 520 Butler Farm Road, Hampton, VA 23666, USA; truong.le@nhrec.org
Received 2011 January 31; accepted 2011 September 6; published 2011 November 21

ABSTRACT

The acceleration of relativistic particles in a viscous accretion disk containing a standing shock is investigated as a possible explanation for the energetic outflows observed around radio-loud black holes. The energy/space distribution of the accelerated particles is computed by solving a transport equation that includes the effects of first-order Fermi acceleration, bulk advection, spatial diffusion, and particle escape. The velocity profile of the accreting gas is described using a model for shocked viscous disks recently developed by the authors, and the corresponding Green's function distribution for the accelerated particles in the disk and the outflow is obtained using a classical method based on eigenfunction analysis. The accretion-driven, diffusive shock acceleration scenario explored here is conceptually similar to the standard model for the acceleration of cosmic rays at supernova-driven shocks. However, in the disk application, the distribution of the accelerated particles is much harder than would be expected for a plane-parallel shock with the same compression ratio. Hence the disk environment plays a key role in enhancing the efficiency of the shock acceleration process. The presence of the shock helps to stabilize the disk by reducing the Bernoulli parameter, while channeling the excess binding energy into the escaping relativistic particles. In applications to M87 and Sgr A*, we find that the kinetic power in the jet is $\sim 0.01\,\dot{M}c^2$, and the outflowing relativistic particles have a mean energy $\sim$300 times larger than that of the thermal gas in the disk at the shock radius. Our results suggest that a standing shock may be an essential ingredient in accretion onto underfed black holes, helping to resolve the long-standing problem of the stability of advection-dominated accretion disks.

Key words: accretion, accretion disks – black hole physics – galaxies: jets

1. INTRODUCTION

The hot, collisionless plasma in advection-dominated accretion flows (ADAFs) around black holes makes them ideal sites for the Fermi acceleration of relativistic particles because the gas is so tenuous that a small fraction of the particles can gain a large amount of energy via multiple interactions with magnetohydrodynamical (MHD) waves. The required velocity dispersion between the waves may be the result of shear flow, random turbulence, or bulk compression. The most efficient possibility is first-order Fermi acceleration due to multiple crossings of a discontinuous shock. Since it has been known for the past two decades that advection-dominated accretion disks can admit dynamical solutions including standing shocks, it is interesting to consider the possible role of shocks in accelerating an energetic population of nonthermal particles which may escape to form the outflows observed in systems containing underfed black holes. In this scenario, the concentrated particle acceleration due to the shock is augmented by additional acceleration resulting from the overall (smooth) convergence of the background flow as it is funneled toward the event horizon.

There are two central questions regarding the possible presence of shocks in advection-dominated disks. The first question is whether the presence of the shock can help to stabilize the disk by reducing the Bernoulli parameter and thereby allowing the remaining gas to accrete. This would solve the problem of the large positive values obtained for the Bernoulli parameter in standard ADAF disks (e.g., Narayan et al. 1997; Blandford & Begelman 1999). The second question is whether shock acceleration is efficient enough to power the outflows observed around underfed black holes. In a series of previous papers, the authors have developed a sequence of self-consistent models for the dynamics and the particle acceleration occurring in inviscid, shocked ADAF disks (Le & Becker 2004, 2005, 2007) and also in viscous disks (Becker et al. 2008; Das et al. 2009). This work helped to establish that shock acceleration in the disk can power the observed outflows in active galaxies and in systems containing stellar-mass black holes.

In the present paper, we continue to investigate the role of standing shocks in hot, tenuous accretion disks in order to understand more fully the nature of the particle acceleration and transport occurring in the disk, and how that is related to the structure of the predicted outflows. The main result presented here is the Green's function energy/space distribution for the accelerated relativistic particles in the disk and the outflow. In that sense, this paper represents the viscous analog to the inviscid model considered by Le & Becker (2007).

The dynamical structures of the accretion flows considered here are computed using the model for viscous, shocked, advection-dominated disks developed by Das et al. (2009), in which the angular momentum transport is governed by the standard Shakura–Sunyaev viscosity prescription (Shakura & Sunyaev 1973). The incorporation of viscosity into the model represents an important step toward the development of a comprehensive understanding of the coupled accretion and outflow processes taking place around underfed black holes. These authors found that in general, shocks can exist in ADAF disks provided the Shakura–Sunyaev viscosity parameter α does not exceed $\sim$0.27, assuming the canonical value $\gamma = 1.5$ for the ratio of the specific heats (e.g., Narayan et al. 1997).

The particle transport scenario we focus on here is analogous to the model for the diffusive acceleration of cosmic rays in supernova shock waves investigated by Blandford & Ostriker (1978) and Jones & Ellison (1991). In that model,

low-energy seed particles are converted to high-energy cosmic rays via multiple shock crossings. The dynamical structure of the shock is determined by the thermodynamics of the background (thermal) plasma, which is the interstellar medium in the supernova/cosmic-ray application. In the disk application, the shock is located at a fixed radius, and the background thermal plasma is provided by the magnetized accreting gas, which passes through the shock on its way to the event horizon. A small population of background particles crosses the shock multiple times due to diffusion, and this leads to the development of a high-energy power-law tail in the particle distribution, which is a natural consequence of the first-order Fermi process (Fermi 1954).

Our study of the particle transport centers on computation of the Green's function describing the evolution of monoenergetic seed particles injected into the disk at a single radius. The solution for the Green's function is obtained by analyzing a cylindrically symmetric transport equation that describes the acceleration and spatial transport of protons and/or electrons. We solve for the Green's function by applying separation of variables combined with eigenfunction analysis based on the asymptotic boundary conditions. The eigenvalues and the corresponding spatial eigenfunctions must be determined numerically because the associated differential equation cannot be solved in closed form. The resulting solution for the Green's function provides a detailed description of the relativistic particle distribution as a function of energy and space. In particular, the solution clearly illustrates how the particle distribution is influenced by advection, spatial diffusion, particle escape, and first-order Fermi acceleration. Based on the solution for the Green's function, we are able to deduce the energy spectrum of the relativistic particles escaping from the disk to form the observed outflows (jets). The energy distribution of the escaping particles is nonthermal in character, with a relatively flat power-law tail.

The remainder of the paper is organized as follows. In Section 2, we briefly review the dynamical model used to describe the structure of the viscous ADAF disk/shock system. In Section 3, we develop the steady-state particle transport equation appropriate for the situation of interest here, and in Section 4 we obtain the general solutions for the associated energy moments. In Section 5, we solve the transport equation for the Green's function describing the evolution of a monoenergetic seed distribution injected at the shock radius, and in Section 6 we evaluate the Green's function and the escaping particle distribution using dynamical parameters appropriate for M87 and Sgr A*. We discuss the astrophysical significance of our results and summarize our main conclusions in Section 7.

2. ACCRETION DYNAMICS

It has been known for some time that standing shocks can exist in inviscid, advection-dominated accretion disks (e.g., Chakrabarti 1989a, 1989b, 1996; Abramowicz & Chakrabarti 1990; Yang & Kafatos 1995; Das et al. 2001). Chakrabarti (1990), Chakrabarti & Das (2004), and Das et al. (2009) demonstrated that shocks can also form in viscous disks if the angular momentum and the viscosity do not exceed critical values. More recently, De Villers et al. (2003) performed detailed general relativistic simulations that confirmed the formation of shocks in the inner region, due to the obstruction of the flow by the centrifugal barrier. Our goal here is to analyze the transport and acceleration of relativistic particles in viscous disks governed by the standard Shakura–Sunyaev viscosity prescription. The specific dynamical model we employ was developed by Das et al. (2009), who characterized the region of the parameter space for the existence of steady-state standing shocks in viscous disks, and also obtained results describing the disk/shock/outflow structures in M87 and Sgr A*.

Le & Becker (2007) pointed out that efficient particle acceleration in the vicinity of a standing shock may power the outflows frequently observed around radio-loud, underfed black holes. This early study focused on inviscid accretion disks, and hence neglected the important role of viscosity in determining the disk structure and regulating the dissipation of energy. Becker et al. (2008) and Das et al. (2009) extended the model to include viscous disks. These studies confirmed that first-order Fermi acceleration inside a viscous, shocked ADAF can accelerate particles more efficiently than in a smooth disk. In the present paper, we continue to extend the earlier results by calculating the detailed particle distributions describing the transport, acceleration, and escape of relativistic particles in the disks around the central black holes in M87 and Sgr A*. We argue that standing shock waves are not only able to power mildly relativistic outflows, but they may actually be required dynamically in order to stabilize the disk and allow the remaining gas to accrete. Furthermore, shocked solutions are expected to possess higher entropy than smooth solutions, and therefore the second law of thermodynamics suggests that when shocked solutions are permitted, they should be expected to form (Becker & Kazanas 2001).

The dynamical effect of the pressure of the accelerated particles is not included in our model for the disk structure, and therefore we are treating the particle transport in the test-particle approximation. This approach parallels that used in the earliest treatments of the diffusive acceleration of cosmic rays at supernova-driven shock fronts (e.g., Blandford & Ostriker 1978). The validity of the test-particle approximation can be examined ex post facto by comparing the resulting pressure of the accelerated relativistic particles with that of the thermal background gas, as discussed in Section 7. In this section, we briefly review the primary dynamical results obtained by Das et al. (2009) before exploring the implications of these results for the transport and acceleration of relativistic particles in the disk.

2.1. Conservation Equations

Within the context of the one-dimensional, steady state, vertically integrated ADAF model of interest here, the accretion rate $\dot{M}$ and the angular momentum transport rate $\dot{J}$ are conserved quantities given by

$$\dot{M} = 4\pi r H \rho v \qquad \dot{J} = \dot{M} r^2 \Omega - \mathcal{G}, \tag{1}$$

respectively, where ρ denotes the mass density, v is the radial component of the flow velocity (defined to be positive for inflow), H represents the disk half-thickness, Ω denotes the angular velocity, and $\mathcal{G}$ represents the torque. The angular velocity gradient $d\Omega/dr$ is related to the torque via (e.g., Frank et al. 2002)

$$\mathcal{G}(r) = -4\pi r^3 H \rho \nu \frac{d\Omega}{dr}, \qquad \nu = \frac{\alpha a^2}{\Omega_{\rm K}}, \tag{2}$$

where the kinematic viscosity ν is computed using the standard Shakura–Sunyaev prescription with constant α.

The vertical hydrostatic structure of the disk is described by the standard expression

$$H(r) = \frac{a}{\Omega_K}, \quad a^2(r) = \frac{P}{\rho}, \tag{3}$$

where a denotes the isothermal sound speed, P is the pressure of the thermal gas, and Ω_K represents the Keplerian angular velocity in the pseudo-Newtonian potential (Paczyński & Wiita 1980), defined by

$$\Omega_K^2(r) \equiv \frac{GM}{r(r-R_S)^2} = \frac{\ell_K^2(r)}{r^4}, \tag{4}$$

for a black hole with mass M and Schwarzschild radius $R_S = 2R_g = 2\,GM/c^2$.

The angular momentum per unit mass transported toward the horizon, ℓ_0, is given by

$$\ell_0 = \frac{\dot{J}}{\dot{M}} = r^2\,\Omega - \frac{\mathcal{G}}{\dot{M}}, \tag{5}$$

which is a conserved quantity throughout the disk in our model. Since the torque $\mathcal{G}$ vanishes at the event horizon as a consequence of general relativity, it follows that ℓ_0 equals the specific angular momentum of the material entering the black hole, i.e.,

$$\ell_0 \equiv \ell(r)\Big|_{r=R_S}, \qquad \ell(r) \equiv r^2\,\Omega(r). \tag{6}$$

The differential equation governing the angular velocity Ω is obtained by combining Equations (1), (2), and (5), which yields

$$\frac{d\Omega}{dr} = \frac{v\,\Omega_K(\ell_0 - r^2\Omega)}{\alpha\,a^2 r^2}. \tag{7}$$

2.2. Entropy Equation

The effect of viscous dissipation on the entropy of the background gas is described by the equation

$$v\,\frac{d}{dr}\ln\left(\frac{U}{\rho^\gamma}\right) = -\frac{\rho\,v\,r^2}{U}\left(\frac{d\Omega}{dr}\right)^2 = -\frac{\alpha(\gamma-1)\,r^2}{\Omega_K}\left(\frac{d\Omega}{dr}\right)^2, \tag{8}$$

where U is the internal energy density of the thermal gas, $\gamma \equiv (U+P)/U$ denotes the ratio of specific heats, and the final result follows from Equations (2) and (3). We set $\gamma = 1.5$ in our numerical examples since it is expected that the magnetic field strength will be close to the equipartition value in underluminous disks (e.g., Narayan et al. 1997). In the absence of viscous dissipation, the right-hand side of Equation (8) vanishes, and we obtain $U \propto \rho^\gamma$, as expected for adiabatic flow. The entropy equation can also be written as

$$v\,\frac{d}{dr}\ln K = -\frac{\alpha\,r^2}{\Omega_K}\left(\frac{d\Omega}{dr}\right)^2, \tag{9}$$

where $K(r)$ is the dimensionless "entropy function" (see Das et al. 2009), given by

$$K(r) \equiv \frac{r\,v}{\Omega_K R_g^2}\left(\frac{a}{c}\right)^{(\gamma+1)/(\gamma-1)} \propto \left(\frac{U}{\rho^\gamma}\right)^{\frac{1}{\gamma-1}}, \tag{10}$$

where $R_g \equiv GM/c^2 = R_S/2$. Note that K remains constant in adiabatic regions, for example, close to the event horizon, where viscous dissipation is negligible. The entropy per particle S is related to K via (Le & Becker 2005)

$$S = k\,\ln K + c_0, \tag{11}$$

where k is Boltzmann's constant and the parameter c_0 depends on the composition of the gas but is independent of its state.

2.3. Wind Equation

The conservation equation for the radial component of the momentum is given by

$$v\,\frac{dv}{dr} = -\frac{1}{\rho}\,\frac{dP}{dr} + r\left(\Omega^2 - \Omega_K^2\right), \tag{12}$$

or, equivalently,

$$v\,\frac{dv}{dr} = -a^2\,\frac{d}{dr}\ln(\rho a^2) + r\left(\Omega^2 - \Omega_K^2\right). \tag{13}$$

The density ρ can be eliminated by using Equations (1) and (3) to write

$$\rho = \frac{\Omega_K \dot{M}}{4\pi\,r\,a\,v}, \tag{14}$$

which can be combined with Equation (13) to obtain

$$\frac{v'}{v}\left(\frac{v^2}{a^2} - 1\right) = \frac{1}{r} - \frac{a'}{a} - \frac{\Omega_K'}{\Omega_K} + \frac{r\left(\Omega^2 - \Omega_K^2\right)}{a^2}, \tag{15}$$

where primes denote differentiation with respect to r.

Using Equation (14) to substitute for ρ in the entropy Equation (8) yields, after some algebra,

$$\left(\frac{\gamma+1}{\gamma-1}\right)\frac{a'}{a} + \frac{v'}{v} + \frac{1}{r} - \frac{\Omega_K'}{\Omega_K} = -\frac{\alpha\,r^2}{v\,\Omega_K}\left(\frac{d\Omega}{dr}\right)^2. \tag{16}$$

By eliminating a' between Equations (15) and (16) and substituting for Ω' using Equation (7), we obtain the differential "wind equation" (e.g., Narayan et al. 1997)

$$\left(\frac{v^2}{a^2} - \frac{2\gamma}{\gamma+1}\right)\frac{v'}{v} = \frac{r(\Omega^2 - \Omega_K^2)}{a^2} + \frac{2\gamma}{\gamma+1}\left(\frac{1}{r} - \frac{\Omega_K'}{\Omega_K}\right) + \left(\frac{\gamma-1}{\gamma+1}\right)\frac{v\,\Omega_K(r^2\Omega - \ell_0)^2}{\alpha r^2 a^4}, \tag{17}$$

which is the fundamental differential equation describing the transonic radial accretion of matter toward the horizon. The final transport rate in the model is that describing the radial propagation of the total energy, given by

$$\dot{E} = -\mathcal{G}\,\Omega + \dot{M}\left(\frac{1}{2}\,r^2\Omega^2 + \frac{1}{2}\,v^2 + \frac{P+U}{\rho} + \Phi\right), \tag{18}$$

where the pseudo-Newtonian potential Φ is defined by (Paczyński & Wiita 1980)

$$\Phi(r) \equiv \frac{-GM}{r - R_S}. \tag{19}$$

By using Equation (5) to eliminate the torque $\mathcal{G}$ in Equation (18) and also utilizing Equation (3), we find that the energy transport rate per unit mass can be written as

$$\epsilon \equiv \frac{\dot{E}}{\dot{M}} = \frac{1}{2}\,v^2 - \frac{1}{2}\,r^2\Omega^2 + \ell_0\,\Omega + \frac{\gamma}{\gamma-1}\,a^2 + \Phi. \tag{20}$$

This relation allows the calculation of a for given values of v and Ω, and it therefore closes the system when combined with Equations (7) and (17). The transport rates $\dot{M}$, $\dot{J}$, and $\dot{E}$ are all defined to be positive for inflow, and in general they are all conserved throughout the disk, although the energy transport rate $\dot{E}$ will display a discontinuous jump at the location of an isothermal shock if one is present in the flow.

In order to obtain global solutions for the flow variables $v(r)$, $a(r)$, and $\Omega(r)$, we must numerically integrate Equations (7), (17), and (20) with respect to radius beginning at the inner radius, $r_{\rm min}$, which is located close to the event horizon. The velocity profile $v(r)$ must be well-behaved throughout the disk, and therefore if the left-hand side of Equation (17) vanishes at some radius, then the right-hand side must vanish at the same radius, which is referred to as a critical point. The infalling gas must pass through at least one critical in the outer region, where the flow transitions from subsonic to supersonic, since general relativity requires supersonic inflow at the event horizon (Weinberg 1972). If the flow is smooth (shock-free), then there is only one critical point, located at radius $r = r_c$. On the other hand, if a shock is present in the flow, then the gas must pass through one critical point in the outer (pre-shock) region at $r = r_c^{\rm out}$, and through another critical point in the inner (post-shock) region at $r = r_c^{\rm in}$ (e.g., Abramowicz & Chakrabarti 1990). The detailed solution procedure is discussed by Das et al. (2009), including the determination of the critical structure of the flow and the application of the inner boundary conditions required to establish the starting values for the flow variables near the horizon.

2.4. Global Dynamical Solutions

A global dynamical model for the structure of the disk/outflow system in a particular source can be developed whenever observational values are available for the black hole mass, M, the accretion rate, $\dot{M}$, and the jet kinetic luminosity, $L_{\rm jet}$. In general, the determination of the structure of an accretion disk containing a shock is a more complex problem than for smooth disks due to the additional restrictions imposed by the shock jump conditions, which tend to reduce the region of the parameter space admitting steady-state dynamical solutions. The process begins with the selection of input values for the three fundamental free parameters for the model, namely the viscosity constant, α, the specific heat ratio, γ, and the specific energy transport rate for the gas supplied at a large radius, denoted by ϵ_-. Based on these fundamental free parameters, we utilize an iteration procedure to compute the specific angular momentum at the horizon, ℓ_0, and the entropy parameter at the horizon, K_0, defined by (see Equation (10))

$$K_0 \equiv K(r)\Big|_{r=R_{\rm S}} . \tag{21}$$

The constants ℓ_0 and K_0 are initially set equal to provisional values and are thereafter iterated until the required boundary and critical conditions are satisfied. Corresponding values for v and Ω at the starting radius $r_{\rm min} = 2.001\,GM/c^2$ are computed using the asymptotic expressions derived by Becker & Le (2003). Equations (7), (17), and (20) are then integrated numerically in the outward direction, beginning at $r = r_{\rm min}$, and the value of K_0 is varied until the left- and right-hand sides of the "wind equation" (Equation (17)) vanish at the same radius, which is identified as the inner critical point, at radius $r_c^{\rm in}$.

When a shock is present, we use the subscripts "−" and "+" to refer to quantities measured just upstream and just downstream from the shock, respectively. The specific energy transport rate ϵ drops from the upstream value ϵ_- to the downstream value ϵ_+ as the gas crosses the shock, reflecting the escape of energy from the disk into the outflow. Since no energy is lost from the disk between the shock and the horizon, it follows that $\epsilon_0 = \epsilon_+$, where ϵ_0 represents the accreted specific energy. In order for the dynamical model to be consistent with the energetics of a particular source, we must require that the power lost from the disk at the isothermal shock location is related to the observed jet kinetic luminosity, $L_{\rm jet}$, via

$$L_{\rm jet} = -\dot{M}\,\Delta\epsilon, \qquad \Delta\epsilon \equiv \epsilon_+ - \epsilon_-, \qquad \epsilon_0 = \epsilon_+, \tag{22}$$

where the negative sign appears because $\Delta\epsilon < 0$. Equation (22) is used to calculate the value of the accreted specific energy ϵ_0 for a specific source based on the input value of ϵ_-.

Another, independent expression for $\Delta\epsilon$ can also be derived from the isothermal shock jump conditions, which can be written as (e.g., Chakrabarti 1989a)

$$\frac{v_+}{v_-} = \mathcal{M}_+^2 = \mathcal{M}_-^{-2}, \qquad \Delta\epsilon = \frac{v_+^2 - v_-^2}{2}, \tag{23}$$

where $\mathcal{M}_- = v_-/a_-$ and $\mathcal{M}_+ = v_+/a_+$ denote the pre- and post-shock Mach numbers, respectively. We determine the shock radius, denoted by r_*, by requiring that the values of $\Delta\epsilon$ computed using Equations (22) and (23) agree. Note that if no shock is present, then ϵ is continuous throughout the entire flow, and consequently $\Delta\epsilon = 0$ and $\epsilon_0 = \epsilon_+ = \epsilon_-$. By definition, the flow maintains a uniform temperature across the isothermal shock, and therefore $a_+ = a_-$.

After the shock location has been determined, the integration continues into the upstream (supersonic) region. The entire integration process, beginning at the starting radius $r_{\rm min}$, is repeated using different values for the accreted specific angular momentum, ℓ_0, until the solution passes smoothly through the outer critical point, located at radius $r_c^{\rm out}$. For a given set of input parameters ϵ_-, α, and γ, at the end of the procedure one obtains unique values for ϵ_0, ℓ_0, K_0, r_*, $r_c^{\rm in}$, and $r_c^{\rm out}$, in addition to the associated global dynamical profiles for the inflow velocity $v(r)$, the angular velocity $\Omega(r)$, and the isothermal sound speed $a(r)$, hence providing a complete physical description of the disk/shock/outflow structure. Das et al. (2009) used this approach to model the dynamics of the accretion disks and the associated outflows in M87 and Sgr A*. In the next section, we develop and analyze the associated transport equation governing the evolution of the relativistic particle distribution resulting from the injection of monoenergetic seed particles.

3. TRANSPORT EQUATION

The role of the shock in accelerating a significant population of nonthermal relativistic particles has been examined in the inviscid case by Le & Becker (2005), who established that the process is capable of powering the outflows observed in both active galaxies and stellar-mass black hole systems. Chakrabarti & Das (2004), Lu et al. (1999), and Chakrabarti (1990) analyzed the consequences of a standing shock for the *heating of the thermal background gas* in the post-shock region of a viscous disk. However, no comprehensive study of the implications of the shock for the *acceleration of nonthermal particles* in viscous disks has yet been undertaken. The acceleration of nonthermal particles can occur very efficiently in hot, tenuous ADAF disks because the plasma is collisionless (Le & Becker

2005), and therefore a small fraction of the particles crosses the shock multiple times, producing the power-law energy spectrum characteristic of Fermi acceleration. In this section, we provide an overview of the transport equation used to model the nonthermal particle acceleration occurring in the disk.

In the steady-state situation considered here, the nonthermal (relativistic) particle distribution is described by the Green's function, $f_{\rm G} \propto {\rm erg}^{-3}\,{\rm cm}^{-3}$, representing the steady-state injection of monoenergetic seed particles subject to acceleration, diffusion, and advection inside the hot tenuous disk. The Green's function is governed by the fundamental transport equation

$$\frac{\partial f_{\rm G}}{\partial t} = 0 = -\vec{\nabla}\cdot\vec{F} - \frac{1}{3E^2}\,\frac{\partial}{\partial E}(E^3\vec{v}\cdot\vec{\nabla} f_{\rm G}) + \dot{f}_{\rm source} - \dot{f}_{\rm esc}, \quad (24)$$

where the specific particle flux $\vec{F}$ is given by

$$\vec{F} = -\kappa\vec{\nabla} f_{\rm G} - \vec{v}\,\frac{E}{3}\,\frac{\partial f_{\rm G}}{\partial E}, \quad (25)$$

and κ and $\vec{v}$ denote the spatial diffusion coefficient and the vector velocity, respectively. The second term on the right-hand side of Equation (24) represents the differential work performed on the relativistic particles by the MHD waves in the convergent background flow. The total number density n_r and energy density U_r of the relativistic particles are related to the Green's function via

$$n_r(r) = \int_0^\infty 4\pi E^2\, f_{\rm G}(E,r)\,dE,$$
$$U_r(r) = \int_0^\infty 4\pi E^3\, f_{\rm G}(E,r)\,dE, \quad (26)$$

which establishes the normalization of $f_{\rm G}$.

Equations (24) and (25) can be combined to rewrite the transport equation in the standard form

$$\vec{v}\cdot\vec{\nabla} f_{\rm G} = \frac{E}{3}\,\frac{\partial f_{\rm G}}{\partial E}\,\vec{\nabla}\cdot\vec{v} + \vec{\nabla}\cdot(\kappa\,\vec{\nabla} f_{\rm G}) + \dot{f}_{\rm source} - \dot{f}_{\rm esc}. \quad (27)$$

The left-hand side of Equation (27) represents the comoving (advective) time derivative and the terms on the right-hand side describe first-order Fermi acceleration, spatial diffusion, particle sources, and the escape of particles through the upper and lower surfaces of the disk, respectively. The velocity has components given by $\vec{v} = v_r\hat{r} + v_z\hat{z} + v_\phi\,\hat{\phi}$, with $v_r = -v < 0$. Note that the transport equation does not include synchrotron or inverse-Compton losses, and therefore it is not expected to describe the acceleration of highly relativistic electrons. Equation (27) was used previously by Becker et al. (2008) to calculate the energy distribution of the relativistic particles escaping from the disk to form the observed outflows in M87. We provide further details of that calculation here and also extend the model to treat the Galactic center source Sgr A*.

In ADAF disks, both the spatial transport and the acceleration of the relativistic particles are regulated by collisions with MHD waves propagating through the thermal background plasma, and therefore the width of the shock is expected to be comparable to the magnetic coherence length, $\lambda_{\rm mag}$. The spatial diffusion coefficient κ is related to $\lambda_{\rm mag}$ via the standard expression $\kappa = c\,\lambda_{\rm mag}/3$, and the shock can be treated as a discontinuity provided $\lambda_{\rm mag} \ll r$. The source function $\dot{f}_{\rm source}$ appearing in Equation (27) describing the injection of monoenergetic seed particles is given by

$$\dot{f}_{\rm source} = \frac{\dot{N}_0\,\delta(E-E_0)\,\delta(r-r_*)}{(4\pi E_0)^2\,r_*\,H_*}, \quad (28)$$

where $H_* \equiv H(r_*)$ denotes the disk half-thickness at the shock location, E_0 represents the energy of the injected particles, and $\dot{N}_0$ is the seed particle injection rate. The seed particles are assumed to originate in the tail of the Maxwellian distribution of the thermal background gas. The model considered here does not include any energy loss mechanism, and therefore all of the particles in the disk (or escaping from it) have energy $E \geqslant E_0$.

The escape of particles via spatial diffusion through the upper and lower surfaces of the disk is represented in Equation (27) by the term

$$\dot{f}_{\rm esc} = A_0\,c\,\delta(r-r_*)\,f_{\rm G}, \quad (29)$$

where the dimensionless constant A_0 determines the importance of particle escape. Based on analysis of the three-dimensional random walk of the escaping particles, Le & Becker (2005) demonstrated that

$$A_0 = \left(\frac{3\kappa_*}{cH_*}\right)^2 < 1, \quad (30)$$

and $\kappa_* \equiv (\kappa_- + \kappa_+)/2$ is the mean value of the spatial diffusion coefficient at $r = r_*$. The condition $A_0 < 1$ is required for the validity of the diffusive treatment of the vertical escape employed in our approach. Most of the particles that escape from the disk are expected to emanate from the region surrounding the shock because the efficiency of the first-order Fermi acceleration is highest there. The localization of the particle escape near the shock radius is represented approximately using the δ-function in Equation (29). The self-consistency of this approximation will be examined in Section 7.

After the velocity profile has been determined using the procedure summarized in Section 2.4, we can compute the Green's function describing the energy and space distribution of the accelerated relativistic particles inside the disk by solving Equation (27). Following Le & Becker (2007), we set the injection energy using $E_0 = 0.002$ erg, which corresponds to an injected Lorentz factor $\Gamma_0 \equiv E_0/(m_p\,c^2) \approx 1.33$, where m_p is the proton mass. The seed particles with initial energy E_0 are picked up from the high-energy tail of the local Maxwellian distribution, and subsequently accelerated to high energies via multiple shock crossings. The Maxwellian seed particles may also be pre-accelerated due to magnetic reconnection at the shock location, triggered by the density discontinuity. The speed of the injected particles, $v_0 = c\,(1-\Gamma_0^{-2})^{1/2}$, exceeds the mean ion thermal velocity at the shock location, $v_{\rm rms} = (3kT_*/m_p)^{1/2}$, by a factor of 3–4, where T_* is the ion temperature at the shock.

In order to maintain a steady-state energy balance in the disk, the energy source associated with the injection of the seed particles must be equal to the rate at which energy is lost from the background plasma into the jet, given by Equation (22). Hence the particle source must be concentrated at the shock location, as reflected by the radial δ-function in Equation (28). With E_0 specified, we can compute the particle injection rate $\dot{N}_0$ using the energy conservation condition (cf. Equation (22))

$$\dot{N}_0\,E_0 = -\dot{M}\,\Delta\epsilon = L_{\rm jet}. \quad (31)$$

We must also specify the radial variation of the spatial diffusion coefficient κ in order to close the system of equations. Following

the approach taken by Le & Becker (2004, 2005, 2007), we adopt the general form

$$\kappa(r) = B_0\, v(r)\, R_{\rm S} \left(\frac{r}{R_{\rm S}} - 1\right)^2, \tag{32}$$

where $R_{\rm S} = 2R_g = 2GM/c^2$, and $B_0 > 0$ is a dimensionless positive constant. In Section 4.5, we show that the value of B_0 can be computed by imposing a global energy balance condition. The presence of the radial speed v in Equation (32) causes κ to be discontinuous at the shock. This is a reasonable behavior since the MHD waves scattering the particles are likely to experience a density compression at the shock that is comparable to that of the background gas. By combining Equations (30) and (32), we find that the dimensionless escape parameter A_0 is given by

$$A_0 = \left(\frac{3B_0 v_* R_{\rm S}}{cH_*}\right)^2 \left(\frac{r_*}{R_{\rm S}} - 1\right)^4 < 1, \tag{33}$$

where $v_* \equiv (v_- + v_+)/2$ is the mean flow speed at the shock. The diffusion parameter B_0 must satisfy the inequality given by Equation (33) in order to ensure the validity of the diffusion approximation we have employed in our treatment of the vertical escape process.

The disk is assumed to be cylindrically symmetric, and therefore we can combine Equations (24), (28), and (29) to obtain

$$v_r \frac{\partial f_{\rm G}}{\partial r} + v_z \frac{\partial f_{\rm G}}{\partial z} = \frac{E}{3}\frac{\partial f_{\rm G}}{\partial E}\left[\frac{1}{r}\frac{d}{dr}(rv_r) + \frac{dv_z}{dz}\right] + \frac{1}{r}\frac{\partial}{\partial r}\left(r\kappa\frac{\partial f_{\rm G}}{\partial r}\right) + \frac{\dot{N}_0\,\delta(E - E_0)\,\delta(r - r_*)}{(4\pi E_0)^2\, r_* H_*} - A_0\, c\,\delta(r - r_*)\, f_{\rm G}. \tag{34}$$

The vertically integrated form of the transport equation can be written as (see Le & Becker 2005, Appendix A)

$$-Hv\frac{\partial f_{\rm G}}{\partial r} = -\frac{1}{r}\frac{d}{dr}(rHv)\frac{E}{3}\frac{\partial f_{\rm G}}{\partial E} + \frac{1}{r}\frac{\partial}{\partial r}\left(rH\kappa\frac{\partial f_{\rm G}}{\partial r}\right) + \frac{\dot{N}_0\,\delta(E - E_0)\,\delta(r - r_*)}{(4\pi E_0)^2 r_*} - A_0\, c\, H_*\,\delta(r - r_*)\, f_{\rm G}, \tag{35}$$

where $v = -v_r > 0$, and $f_{\rm G}$, κ, and v will denote vertically averaged functions throughout the remainder of the paper. The first-order Fermi acceleration of the particles is concentrated near the shock, where v is discontinuous, and the velocity derivative is singular, i.e.,

$$\frac{dv}{dr} \to (v_- - v_+)\,\delta(r - r_*), \qquad r \to r_*, \tag{36}$$

where v_- and v_+ represent the (positive) inflow speeds just upstream and downstream from the shock, respectively. The strong Fermi acceleration near the shock is augmented by additional acceleration occurring in the surrounding region due to the general convergence of the MHD waves in the accretion flow.

4. VARIATION OF THE ENERGY MOMENTS

Our primary goal in this paper is to calculate the Green's function describing the particle distribution resulting from the continual injection of monoenergetic seed particles from a source located at the shock radius. In order to validate the solution obtained for the particle distribution, it is useful to have available separate solutions for the "energy moments" of the Green's function, $I_n(r)$, defined by

$$I_n(r) \equiv \int_0^\infty 4\pi E^n\, f_{\rm G}(E, r)\, dE. \tag{37}$$

The two most interesting examples are I_2 and I_3, which are related to the relativistic particle number and energy densities via (cf. Equations (26))

$$n_r(r) = I_2(r), \qquad U_r(r) = I_3(r). \tag{38}$$

By operating on Equation (35) with $\int_0^\infty 4\pi E^n\, dE$ and integrating by parts, we find that the nth energy moment satisfies the vertically integrated differential equation

$$-Hv\frac{dI_n}{dr} = \left(\frac{n+1}{3}\right)\frac{I_n}{r}\frac{d}{dr}(rHv) + \frac{1}{r}\frac{d}{dr}\left(rH\kappa\frac{dI_n}{dr}\right) + \frac{\dot{N}_0\, E_0^{n-2}\,\delta(r - r_*)}{4\pi\, r_*} - A_0\, c\, H_*\,\delta(r - r_*)\, I_n, \tag{39}$$

which can also be expressed in the flux-conservation form

$$\frac{d}{dr}(4\pi r H F_n) = 4\pi r H\left[\left(\frac{2-n}{3}\right)v\frac{dI_n}{dr} + \frac{\dot{N}_0\, E_0^{n-2}\,\delta(r - r_*)}{4\pi r_* H_*} - A_0\, c\,\delta(r - r_*)\, I_n\right], \tag{40}$$

where $4\pi r H F_n$ represents the rate of radial transport of the nth moment, and the associated radial moment flux F_n is defined by

$$F_n \equiv -\left(\frac{n+1}{3}\right) v\, I_n - \kappa\,\frac{dI_n}{dr}. \tag{41}$$

Once the disk/shock dynamics have been computed based on the selected values for the free parameters ϵ_-, α, and γ using the results in Section 2, the corresponding solutions for the number and energy densities of the relativistic particles in the disk can be obtained by numerically integrating Equation (39).

4.1. Derivative Jump

The solution for I_n displays a derivative jump at the location of the source/shock due to the δ-functions appearing on the right-hand side of Equation (39). The jump condition can be obtained by integrating this equation with respect to radius over a small region surrounding the shock location. For an isothermal shock, with continuous H, this yields

$$\Delta\left(\kappa\,\frac{dI_n}{dr}\right) = \frac{\dot{N}_0\, E_0^{n-2}}{4\pi r_* H_*} - A_0\, c\, I_n(r_*) - \left(\frac{n+1}{3}\right) I_n(r_*)\,\Delta v, \tag{42}$$

where the symbol "Δ" refers to the difference between post- and pre-shock quantities (see Equation (22)). The corresponding jump condition for the radial moment flux F_n is

$$\Delta F_n = A_0\, c\, I_n(r_*) - \frac{\dot{N}_0\, E_0^{n-2}}{4\pi r_* H_*}, \tag{43}$$

obtained by integrating Equation (40).

4.2. Asymptotic Behavior

In order to solve the second-order differential Equation (39) for the moment functions $I_n(r)$, we must introduce two boundary conditions. The required conditions can be developed by analyzing the asymptotic variation of I_n near the event horizon and at large distances from the black hole.

Close to the event horizon, the gas must advect inward at the speed of light, in accordance with general relativity, and therefore diffusion is negligible in this regime. Conversely, far from the horizon, advection is negligible and consequently the particle transport in the disk is dominated by diffusion as $r \rightarrow \infty$. We can use these physical principles to determine the asymptotic variation of the energy moments I_n as follows.

General relativity requires that as $r \rightarrow R_S = 2GM/c^2$, the inflow velocity v must approach the free-fall velocity,

$$v_{ff}(r) = \left(\frac{2GM}{r - R_S}\right)^{1/2}, \tag{44}$$

and therefore we obtain the asymptotic behavior

$$v(r) \propto (r - R_S)^{-1/2}, \qquad r \rightarrow R_S. \tag{45}$$

Note that v diverges as $r \rightarrow R_S$, and therefore it actually represents the radial component of the four-velocity in this limit (see Becker & Le 2003). Since the viscous stress is negligible close to the horizon, viscous dissipation is unimportant, and the flow behaves adiabatically, with $P \propto \rho^\gamma$, in which case Equation (3) yields

$$a(r) \propto \rho^{(\gamma-1)/2}, \qquad r \rightarrow R_S. \tag{46}$$

Incorporating these relations into Equations (1) and (3) and eliminating H, we find that the density variation close to the horizon is given by

$$\rho(r) \propto (r - R_S)^{-1/(\gamma+1)}, \qquad r \rightarrow R_S, \tag{47}$$

in agreement with Equation (55) from Becker & Le (2003).

In the adiabatic region near the horizon, the right-hand side of Equation (39) is dominated by the first term, describing first-order Fermi acceleration, and therefore we obtain

$$-Hv\frac{dI_n}{dr} = \left(\frac{n+1}{3}\right)\frac{I_n}{r}\frac{d}{dr}(rHv), \qquad r \rightarrow R_S. \tag{48}$$

Eliminating H using Equation (1) yields upon integration

$$I_n(r) \propto \rho^{(n+1)/3} \propto (r - R_S)^{-(n+1)/(3\gamma+3)}, \qquad r \rightarrow R_S, \tag{49}$$

where the final result follows from Equation (47). In particular, by setting $n = 2$ or $n = 3$, we find that the asymptotic variations of the relativistic particle number and energy densities close to the horizon are given by the adiabatic relations

$$n_r(r) \propto \rho \propto (r - R_S)^{-1/(\gamma+1)}, \qquad r \rightarrow R_S, \tag{50}$$

$$U_r(r) \propto \rho^{4/3} \propto (r - R_S)^{-4/(3\gamma+3)}, \qquad r \rightarrow R_S. \tag{51}$$

These expressions provide the inner boundary conditions required to solve Equation (39) for $I_2 = n_r$ and $I_3 = U_r$.

Far from the black hole, the sound speed a and the density ρ are expected to approach constant values as the gas merges with the ambient interstellar medium of the host galaxy. It follows from Equations (1), (3), and (4) that H and v display the asymptotic behaviors

$$H(r) \propto r^{3/2}, \quad v(r) \propto r^{-5/2}, \qquad r \rightarrow \infty. \tag{52}$$

The corresponding asymptotic variation of the diffusion coefficient κ is obtained by combining Equations (32) and (52), which yields

$$\kappa(r) \propto r^{-1/2}, \qquad r \rightarrow \infty. \tag{53}$$

In this limit, the particle transport is dominated by outwardly directed diffusion, and therefore bulk advection and Fermi acceleration are negligible. We therefore conclude that Equation (39) reduces to

$$\frac{1}{r}\frac{d}{dr}\left(rH\kappa\frac{dI_n}{dr}\right) = 0, \qquad r \rightarrow \infty. \tag{54}$$

Based on Equations (52), (53), and (54), one can show that at large radii, the asymptotic variation of the moment function I_n is given by

$$I_n(r) \propto \frac{1}{H\kappa} \propto r^{-1}, \qquad r \rightarrow \infty. \tag{55}$$

It follows that the two outer boundary conditions required to solve Equation (39) for $I_2 = n_r$ and $I_3 = U_r$ are given by

$$n_r(r) \propto r^{-1}, \qquad r \rightarrow \infty, \tag{56}$$

$$U_r(r) \propto r^{-1}, \qquad r \rightarrow \infty. \tag{57}$$

4.3. Formal Solution

The global solution for $I_n(r)$ can now be expressed as

$$I_n(r) = \begin{cases} A\ Q_I(r), & r \geqslant r_*, \\ B\ Q_{II}(r), & r \leqslant r_*, \end{cases} \tag{58}$$

where A and B are constants and the functions $Q_I(r)$ and $Q_{II}(r)$ satisfy the homogeneous differential equation (see Equation (39))

$$-Hv\frac{dQ}{dr} = \left(\frac{n+1}{3}\right)\frac{Q}{r}\frac{d}{dr}(rHv) + \frac{1}{r}\frac{d}{dr}\left(rH\kappa\frac{dQ}{dr}\right), \tag{59}$$

which can be rewritten as

$$\frac{d^2Q}{dr^2} + \left[\frac{d\ln(rH\kappa)}{dr} + \frac{v}{\kappa}\right]\frac{dQ}{dr} + \frac{(n+1)\,v}{3\,\kappa}\frac{d\ln(rHv)}{dr}Q = 0. \tag{60}$$

Physically acceptable solutions to this equation must also satisfy the asymptotic boundary conditions given by Equations (49) and (55), and therefore we require that

$$Q_I(r)\Big|_{r=r_{max}} = \left(\frac{r_{max}}{R_S}\right)^{-1},$$

$$Q_{II}(r)\Big|_{r=r_{min}} = \left(\frac{r_{min}}{R_S} - 1\right)^{-(n+1)/(3\gamma+3)}, \tag{61}$$

where r_{min} and r_{max} denote the radii at which the inner and outer boundary conditions are applied, respectively. In our calculations, we set $r_{min} = 2.001\ R_g$ and $r_{max} = 10^5\ R_g$.

By substituting for $\kappa(r)$ using Equation (32), we can rewrite Equation (59) in the alternative form

$$\frac{d^2Q}{dr^2} + \left[\frac{d\ln(rHv)}{dr} + \frac{2}{r-R_S} + \frac{R_S}{B_0(r-R_S)^2}\right]\frac{dQ}{dr} + \frac{(n+1)\,R_S\,Q}{3B_0(r-R_S)^2}\,\frac{d\ln(rHv)}{dr} = 0. \quad (62)$$

In order to solve this equation, we require knowledge of the velocity profile $v(r)$ and the disk half-thickness $H(r)$. By combining Equations (3) and (10), we find that

$$H(r) = \frac{c}{\Omega_K(r)}\left[\frac{K\Omega_K(r)R_g^2}{r\,v(r)}\right]^{(\gamma-1)/(\gamma+1)}, \quad (63)$$

where Ω_K is the pseudo-Newtonian angular velocity and K is the entropy function, which is discontinuous at the shock but is otherwise constant (see Becker & Le 2003). Hence the variation of $H(r)$ can be computed once a dynamical solution for $v(r)$ has been obtained using the procedure discussed in Section 2. This allows us to evaluate all of the coefficients in Equation (62), and therefore the solutions for $Q_I(r)$ and $Q_{II}(r)$ can be obtained via numerical integration in combination with the inner and outer boundary conditions given by Equations (61).

The constants A and B in Equation (58) are calculated by requiring that I_n be continuous at $r = r_*$ and that the derivative dI_n/dr comply with the jump condition given by Equation (42). After some algebra, we obtain

$$A = B\,\frac{Q_{II}}{Q_I}\bigg|_{r=r_*}, \quad (64)$$

$$B = \frac{\dot{N}_0\,E_0^{n-2}}{4\pi r_* H_* Q_{II}}\left[\frac{n+1}{3}\,(v_+ - v_-) + \frac{Q'_{II}\kappa_+}{Q_{II}} - \frac{Q'_I\kappa_-}{Q_I} + A_0\,c\right]^{-1}\bigg|_{r=r_*}, \quad (65)$$

where primes denote radial differentiation. The solutions for the functions $Q_I(r)$ and $Q_{II}(r)$ are determined by numerically integrating Equation (60) subject to the asymptotic relations given by Equations (61). Once the constants A and B are obtained using Equations (64) and (65), the global solution for $I_n(r)$ is computed using Equation (58). The escape constant A_0 is evaluated using Equation (33) if a shock exists in the flow; otherwise we set $A_0 = 0$. Hence the formal solution applies whether or not a shock is present.

4.4. Relativistic Particle Number Density

In the case of the relativistic particle number density, $n_r = I_2$, it is interesting to recast Equation (40) in the flux-conservation form

$$\frac{d\dot{N}_r}{dr} = \dot{N}_0\,\delta(r-r_*) - 4\pi r_* H_* A_0\,c\,n_r\,\delta(r-r_*), \quad (66)$$

where $\dot{N}_r(r)$ is the relativistic particle transport rate, expressing the number of particles per second crossing a cylindrical shell at radius r. The transport rate $\dot{N}_r$ is related to the relativistic particle number density, $n_r(r)$, via

$$\dot{N}_r(r) = -4\pi r H\left(v\,n_r + \kappa\,\frac{dn_r}{dr}\right) \propto \mathrm{s}^{-1}. \quad (67)$$

We define $\dot{N}_r(r)$ to be negative if the net particle transport is in the inward direction at radius r. The derivative term in Equation (67) represents the contribution to the particle flux due to spatial diffusion. Since the particle flux must be finite everywhere in the disk, we require that the number density $n_r(r)$ must be a continuous function of r.

The two spatial regions of concern in our calculation are referred to as region I ($r > r_*$) and region II ($r < r_*$). Away from the shock location, $r \neq r_*$, and therefore the right-hand side of Equation (66) vanishes, leaving $\dot{N}_r =$ constant. Hence we find that

$$\dot{N}_r(r) = \begin{cases} \dot{N}_I, & r > r_*, \\ \dot{N}_{II}, & r < r_*, \end{cases} \quad (68)$$

where the constant $\dot{N}_{II} < 0$ is the rate at which particles are transported radially inward toward the event horizon, and the constant $\dot{N}_I > 0$ denotes the rate at which particles are transported radially outward.

Only a small fraction of the injected seed particles escape through the disk surface to form the jet, with the rate of escape denoted by $\dot{N}_{esc} \ll \dot{N}_0$. The majority of the particles are either transported outward to large radii at the rate $\dot{N}_I$, or inward through the event horizon at the rate $\dot{N}_{II}$. The escape rate $\dot{N}_{esc}$ can be computed by integrating Equation (66) with respect to radius in a small region around $r = r_*$, which yields

$$\dot{N}_{esc} = 4\pi r_* H_* A_0\,c\,n_*, \quad (69)$$

where $n_* \equiv n_r(r_*)$. The corresponding jump condition for the particle transport rate at the source location is given by

$$\dot{N}_I - \dot{N}_{II} = \dot{N}_0 - \dot{N}_{esc}. \quad (70)$$

The jump in the value of $\dot{N}_r$ across the source/shock radius gives rise to a corresponding discontinuity in the derivative dn_r/dr via Equation (67). Note that if no shock is present in the flow, then $A_0 = 0$ and consequently $\dot{N}_{esc} = 0$.

4.5. Relativistic Particle Energy Density

The conservation equation for the relativistic particle energy density, $U_r = I_3$, can be recast in the flux-conservation form

$$\frac{d\dot{E}_r}{dr} = 4\pi r H\left[-\frac{v}{3}\frac{dU_r}{dr} + \frac{\dot{N}_0\,E_0\,\delta(r-r_*)}{4\pi r_* H_*} - A_0\,c\,U_r\,\delta(r-r_*)\right], \quad (71)$$

where

$$\dot{E}_r(r) \equiv -4\pi r H\left(\frac{4}{3}\,v\,U_r + \kappa\,\frac{dU_r}{dr}\right) \propto \mathrm{erg\ s}^{-1} \quad (72)$$

denotes the relativistic particle energy transport rate. We define $\dot{E}_r(r)$ to be negative if the net energy transport is in the inward direction at radius r. The value of $\dot{E}_r$ varies throughout the flow due to the action of the first term on the right-hand side of Equation (71), which represents the compressional work done on the relativistic particles by the background flow.

By integrating Equation (71) in a very small region around $r = r_*$, we find that the energy transport rate $\dot{E}_r$ possesses a jump at the shock/source location given by

$$\Delta\dot{E}_r = L_{esc} - \dot{N}_0\,E_0, \quad (73)$$

where

$$L_{\rm esc} \equiv 4\pi r_* H_* A_0\, c\, U_* \;\propto\; {\rm erg\ s^{-1}} \tag{74}$$

represents the rate of escape of particle energy from the disk into the outflow/jet at the shock location, $U_* \equiv U_r(r_*)$, and the symbol "Δ" refers to the difference between post- and pre-shock quantities (see Equation (22)).

The energy density $U_r(r)$ must be a continuous function of the radius r throughout the disk in order to avoid generating an infinite diffusive flux. However, the derivative dU_r/dr will possess a discontinuity at $r = r_*$ due to the jump in the energy transport rate $\dot{E}_r$ indicated by Equation (73). The corresponding derivative jump condition for the energy density at the shock location is given by

$$\Delta\left(\kappa\,\frac{dU_r}{dr}\right) = \frac{\dot{N}_0\, E_0 - L_{\rm esc}}{4\pi r_* H_*} - \frac{4}{3}\,U_*\,\Delta v. \tag{75}$$

If no shock is present, then $A_0 = 0$, and therefore $L_{\rm esc} = 0$ in this case.

A fundamental constraint on the model parameters can be obtained by imposing the global energy conservation condition

$$L_{\rm esc} = \dot{N}_0\, E_0 = -\dot{M}\,\Delta\epsilon, \tag{76}$$

which mandates that the energy lost from the disk per unit time in the form of the escaping relativistic particles is exactly equal to the energy input rate for the seed particles, which in turn is exactly equal to the energy loss rate for the background accretion flow at the shock location. We vary the value of the diffusion constant B_0 (see Equation (32)) until the value of $L_{\rm esc}$ computed using Equation (74) satisfies Equation (76), hence ensuring the global self-consistency of our treatment of energy conservation.

The energy provided in the form of the seed particles is redistributed via first-order Fermi acceleration over a much smaller population of escaping particles, and therefore we anticipate that the mean energy of the escaping particles, $\langle E\rangle$, will greatly exceed the energy of the injected particles, E_0. We can quantify the relationship between these two energies by writing

$$\langle E\rangle = \frac{U_*}{n_*} = \frac{L_{\rm esc}}{\dot{N}_{\rm esc}} = \frac{\dot{N}_0}{\dot{N}_{\rm esc}}\,E_0. \tag{77}$$

Since $\dot{N}_{\rm esc} \ll \dot{N}_0$, it follows that $\langle E\rangle \gg E_0$, as expected. The mean amplification ratio, $\langle E\rangle/E_0$, will provide a useful means for characterizing the efficiency of the particle acceleration process in the specific applications that will be explored later in the paper. By combining Equations (73) and (77), we find that

$$\Delta\dot{E}_r = 0. \tag{78}$$

The relativistic particle energy transport rate $\dot{E}_r$ is continuous at the shock location due to the balance between the energy contained in the injected seed particles and the energy contained in the (smaller) population of escaping, accelerated particles.

5. SOLUTION FOR THE GREEN'S FUNCTION

Equation (35) governs the evolution of the vertically integrated Green's function, $f_{\rm G}$, which describes the response of the system to the continual injection of monoenergetic seed particles with energy E_0 from a source located at radius r_*. Since the fundamental transport equation is linear, it follows that the particular solution for the relativistic particle distribution resulting from any energy/space source distribution can be obtained from the Green's function via convolution. Hence the solution for $f_{\rm G}$ contains the essential physics describing the transport and acceleration of the relativistic particles throughout the disk. In this section, we employ standard methods of mathematical physics to obtain an expression for $f_{\rm G}$ in terms of an orthogonal set of basis functions.

5.1. Separation of Variables

The source term in Equation (35) vanishes for values of the particle energy $E \neq E_0$, and in this case the remaining homogeneous equation may be separated in energy and space by utilizing dimensionless functions of the form

$$f(\lambda, E, r) = \left(\frac{E}{E_0}\right)^{-\lambda}\varphi(\lambda, r), \tag{79}$$

where λ is the separation constant, and the dimensionless spatial functions $\varphi(\lambda, r)$ satisfy the second-order ordinary differential equation

$$-Hv\frac{d\varphi}{dr} = \frac{\lambda}{3r}\frac{d}{dr}(rHv)\,\varphi + \frac{1}{r}\frac{d}{dr}\left(rH\kappa\,\frac{d\varphi}{dr}\right) - A_0\, c\, H_*\,\delta(r - r_*)\,\varphi. \tag{80}$$

Since the coefficients in Equation (80) cannot be represented in closed form, it is not possible to obtain analytical solutions, and therefore the spatial separation functions φ must be determined numerically. Equation (80) can be rearranged to obtain

$$\frac{d^2\varphi}{dr^2} + \left[\frac{d\ln(rH\kappa)}{dr} + \frac{v}{\kappa}\right]\frac{d\varphi}{dr} + \frac{\lambda\, v}{3\,\kappa}\,\frac{d\ln(rHv)}{dr}\,\varphi = \frac{A_0\, c}{\kappa}\,\delta(r - r_*)\,\varphi. \tag{81}$$

The final term on the right-hand side of Equation (81) vanishes away from the shock ($r \neq r_*$), in which case it reduces to the homogeneous equation

$$\frac{d^2\varphi}{dr^2} + \left[\frac{d\ln(rHv)}{dr} + \frac{2}{r - R_{\rm S}} + \frac{R_{\rm S}}{B_0(r - R_{\rm S})^2}\right]\frac{d\varphi}{dr} + \left[\frac{\lambda R_{\rm S}}{3B_0(r - R_{\rm S})^2}\,\frac{d\ln(rHv)}{dr}\right]\varphi = 0, \tag{82}$$

where we have substituted for $\kappa(r)$ using Equation (32), and $H(r)$ is computed using Equation (63) once a dynamical solution for $v(r)$ has been obtained.

5.2. Asymptotic Behavior

Equation (81) is a linear second-order differential equation, and therefore we must impose two physical boundary conditions in order to determine the global solutions for the spatial separation functions φ. These conditions can be easily developed by noting that away from the shock ($r \neq r_*$), Equation (81) is equivalent to Equation (60) if we make the replacement $\lambda \rightarrow n + 1$. Following the same reasoning utilized in Section 4.1, we can immediately conclude based on the adiabatic nature of the flow close to the event horizon and the diffusive nature of the particle transport at large radii that

$$\varphi(\lambda, r) \;\propto\; (r - R_{\rm S})^{-\lambda/(3\gamma+3)}, \qquad r \rightarrow R_{\rm S}, \tag{83}$$

$$\varphi(\lambda, r) \;\propto\; r^{-1}, \qquad r \rightarrow \infty. \tag{84}$$

The global solution for the spatial separation function $\varphi(r)$ can therefore be written as

$$\varphi(\lambda, r) = \begin{cases} a_{\rm I}\, G_{\rm I}(r), & r \geqslant r_*, \\ G_{\rm II}(r), & r \leqslant r_*, \end{cases} \tag{85}$$

where $a_{\rm I}$ is the matching coefficient and $G_{\rm I}(r)$ and $G_{\rm II}(r)$ represent the fundamental solutions to the homogeneous Equation (82) satisfying the boundary conditions (cf. Equations (61))

$$G_{\rm I}(r)\bigg|_{r=r_{\rm max}} = \left(\frac{r_{\rm max}}{R_{\rm S}}\right)^{-1} \quad G_{\rm II}(r)\bigg|_{r=r_{\rm min}} = \left(\frac{r_{\rm min}}{R_{\rm S}} - 1\right)^{-\lambda/(3\gamma+3)}, \tag{86}$$

with $r_{\rm min} = 2.001\, R_g$ and $r_{\rm max} = 10^5\, R_g$ denoting the inner and outer boundary radii for the calculation, respectively. The value of the matching coefficient $a_{\rm I}$ is determined by ensuring the continuity of $\varphi(\lambda, r)$ at $r = r_*$, which yields

$$a_{\rm I} = \frac{G_{\rm II}(r_*)}{G_{\rm I}(r_*)}. \tag{87}$$

5.3. Eigenvalues and Eigenfunctions

By integrating Equation (80) or Equation (81) with respect to radius in the vicinity of the shock, we find that the spatial separation functions $\varphi(\lambda, r)$ must satisfy the derivative jump condition

$$\Delta\left(\kappa\,\frac{d\varphi}{dr}\right) = -\left(A_0\, c + \frac{\lambda}{3}\,\Delta v\right)\varphi(r_*), \tag{88}$$

where the symbol Δ denotes the difference between post-shock and pre-shock quantities and we have utilized the fact that φ is continuous across the shock. The jump condition given by Equation (88) is only satisfied for certain values of λ, and this criterion defines the set of discrete eigenvalues, denoted by λ_n, which form an increasing sequence of positive numbers. The associated spatial eigenfunctions, $\varphi_n(r)$, are defined by

$$\varphi_n(r) \equiv \varphi(\lambda_n, r). \tag{89}$$

The procedure for obtaining the set of eigenvalues and spatial eigenfunctions begins with the integration of Equation (82) in the outward and inward directions, starting with the asymptotic boundary conditions given by Equations (86). This yields solutions for the inner and outer spatial functions $G_{\rm II}(r)$ and $G_{\rm I}(r)$, respectively. The matching coefficient $a_{\rm I}$ is computed by requiring continuity of the solution at the source radius r_* using Equation (87), and the resulting global solution for φ is evaluated using Equation (85). The value of λ is varied until the derivative jump condition (Equation (88)) is satisfied at the shock location. This process establishes the complete set of eigenvalues λ_n and the associated spatial eigenfunctions $\varphi_n(r)$.

5.4. Eigenfunction Orthogonality

Away from the shock ($r \neq r_*$), the spatial eigenfunctions $\varphi_n(r)$ satisfy Equation (82), which can be rewritten in the Sturm–Liouville form

$$\frac{d}{dr}\left[S(r)\,\frac{d\varphi_n}{dr}\right] + \frac{\lambda_n\,\omega(r)}{R_g^2}\,\varphi_n(r) = 0, \tag{90}$$

where $S(r)$ is given by the dimensionless definition

$$S(r) \equiv \frac{r H \kappa}{r_* H_* \kappa_*}\,\exp\left\{\frac{1}{B_0}\left[\left(\frac{r_*}{R_{\rm S}} - 1\right)^{-1} - \left(\frac{r}{R_{\rm S}} - 1\right)^{-1}\right]\right\}, \tag{91}$$

where $\kappa_* \equiv (\kappa_- + \kappa_+)/2$ and the dimensionless weight function $\omega(r)$ is defined by

$$\omega(r) \equiv \frac{2R_g^3\, S(r)}{3B_0(r - R_{\rm S})^2}\,\frac{d\ln(r H v)}{dr}, \tag{92}$$

where $R_g = R_{\rm S}/2 = GM/c^2$. Due to the dependence of $\omega(r)$ on the velocity derivative dv/dr, the weight function possesses a δ-function singularity at the shock location. According to Equation (91), $S(r_*) = 1$, and therefore we can combine Equations (32), (36), and (92) to show that the behavior of the weight function in the vicinity of the shock is given by

$$\omega(r) \to R_g^2\left(\frac{v_- - v_+}{3\kappa_*}\right)\delta(r - r_*), \qquad r \to r_*. \tag{93}$$

Next we employ standard methods to show that the spatial eigenfunctions form an orthogonal set. Consider the eigenfunctions $\varphi_n(r)$ and $\varphi_m(r)$ with distinct eigenvalues λ_n and λ_m, respectively. Since φ_m satisfies Equation (90), we can write

$$\frac{d}{dr}\left[S(r)\,\frac{d\varphi_m}{dr}\right] + \frac{\lambda_m\,\omega(r)}{R_g^2}\,\varphi_m(r) = 0. \tag{94}$$

Multiplying Equation (90) by λ_m and Equation (94) by λ_n and subtracting the first from the second yields

$$\varphi_n(r)\,\frac{d}{dr}\left[S(r)\,\frac{d\varphi_m}{dr}\right] - \varphi_m(r)\,\frac{d}{dr}\left[S(r)\,\frac{d\varphi_n}{dr}\right] = \frac{(\lambda_n - \lambda_m)\,\omega(r)}{R_g^2}\,\varphi_n(r)\,\varphi_m(r). \tag{95}$$

After integrating by parts from $r = R_{\rm S}$ to $r = \infty$ and simplifying, we obtain

$$R_g^2\, S(r)\left[\varphi_n(r)\frac{d\varphi_m}{dr} - \varphi_m(r)\frac{d\varphi_n}{dr}\right]_{R_{\rm S}}^{\infty} = (\lambda_n - \lambda_m)\int_{R_{\rm S}}^{\infty}\omega(r)\,\varphi_n(r)\,\varphi_m(r)\,dr. \tag{96}$$

Based on the boundary conditions for φ given by Equations (83) and (84), we conclude that in the two limits $r \to R_{\rm S}$ and $r \to \infty$, the left-hand side of Equation (96) vanishes, leaving the standard orthogonality relation

$$\int_{R_{\rm S}}^{\infty}\varphi_n(r)\,\varphi_m(r)\,\omega(r)\,dr = 0, \qquad m \neq n. \tag{97}$$

This result confirms that the family of spatial eigenfunctions $\varphi_n(r)$ form an orthogonal set relative to the weight function $\omega(r)$ given by Equation (92).

5.5. Orthonormal Expansion

The integral relation given by Equation (97) implies that the spatial separation functions $\varphi_n(r)$ form a complete set, as expected for a standard Sturm–Liouville problem. We can therefore express the Green's function $f_{\rm G}$ using the expansion (see Equation (79))

$$f_{\rm G}(E, r) = \sum_{n=1}^{N_{\rm max}} b_n \varphi_n(r)\left(\frac{E}{E_0}\right)^{-\lambda_n}, \qquad E \geqslant E_0, \tag{98}$$

where the b_n constants are the expansion coefficients and $N_{\max}$ is the index of the largest eigenvalue considered in the summation, based on analysis of the term-by-term convergence of the series. In our numerical examples, we generally set $N_{\max} = 10$, which typically yields about three decimal digits of accuracy in the solution for $f_{\rm G}$. The eigenvalues form an increasing sequence of positive numbers, and therefore the dominant behavior at high energies is given by the first eigenvalue, λ_1. In order to obtain a finite result for the total energy density of the accelerated relativistic particles, U_r, we must require that $\lambda_1 > 4$ (see Equation (3)).

We can compute the expansion coefficients b_n by exploiting the orthogonality of the spatial eigenfunctions $\varphi_n(r)$. At the source energy, $E = E_0$, Equation (98) reduces to

$$f_{\rm G}(E_0, r) = \sum_{m=1}^{N_{\max}} b_m \, \varphi_m(r). \tag{99}$$

Multiplying both sides of this equation by $\varphi_n(r)\,\omega(r)$ and integrating with respect to radius from $r = R_{\rm S}$ to $r = \infty$ yields

$$\int_{R_{\rm S}}^{\infty} f_{\rm G}(E_0, r)\,\varphi_n(r)\,\omega(r)\,dr = \sum_{m=1}^{N_{\max}} b_m \int_{R_{\rm S}}^{\infty} \varphi_m(r)\,\varphi_n(r)\,\omega(r)\,dr. \tag{100}$$

The orthogonality relation (Equation (97)) implies that only the $m = n$ term in the sum survives on the right-hand side of Equation (100), and therefore we obtain

$$\int_{R_{\rm S}}^{\infty} f_{\rm G}(E_0, r)\,\varphi_n(r)\,\omega(r)\,dr = b_n \int_{R_{\rm S}}^{\infty} \varphi_n^2(r)\,\omega(r)\,dr, \tag{101}$$

which yields for the expansion coefficient b_n the result

$$b_n = \frac{\int_{R_{\rm S}}^{\infty} f_{\rm G}(E_0, r)\,\varphi_n(r)\,\omega(r)\,dr}{R_g\,\mathcal{I}_n}, \tag{102}$$

where the dimensionless quadratic normalization integrals, $\mathcal{I}_n$, are defined by

$$\mathcal{I}_n \equiv \frac{1}{R_g}\int_{R_{\rm S}}^{\infty} \varphi_n^2(r)\,\omega(r)\,dr. \tag{103}$$

In order to compute the integrals in Equation (102), we need to evaluate the Green's function at the source energy, $f_{\rm G}(E_0, r)$. An expression for $f_{\rm G}(E_0, r)$ can be obtained by substituting for the velocity derivative in Equation (35) using Equation (36) and subsequently integrating with respect to energy in a small range around the injection energy E_0, which yields

$$f_{\rm G}(E_0, r) = \begin{cases} \dfrac{3\dot{N}_0}{(4\pi)^2 E_0^3\, r_*\, H_*(v_- - v_+)}, & r = r_*, \\ 0, & r \neq r_*. \end{cases} \tag{104}$$

Note that $f_{\rm G}(E, r) = 0$ for all $E < E_0$, because no deceleration processes are included in the particle transport model considered here. In the Blandford & Ostriker (1978) model for the diffusive acceleration of cosmic rays in a plane-parallel supernova shock wave, the Green's function evaluated at the injection energy E_0 has a finite value at all locations in the flow, because there is no convergence in the plasma away from the shock. By contrast, in the model considered here, the MHD scattering centers converge at all radii due to the general convergence of the accretion flow in the disk. This additional, distributed particle acceleration causes the Green's function to vanish at the injection energy for all $r \neq r_*$.

Substituting for $f_{\rm G}(E_0, r)$ in Equation (102) using Equation (104) and performing the required radial integration, we find that

$$b_n = \frac{\dot{N}_0\, R_g\, \varphi_n(r_*)}{(4\pi)^2 E_0^3\, r_*\, H_*\, \kappa_*\, \mathcal{I}_n} \;\propto\; \mathrm{erg}^{-3}\,\mathrm{cm}^{-3} \tag{105}$$

where we have accounted for the δ-function behavior of the weight function $\omega(r)$ in the vicinity of the shock (see Equation (93)). This effect also needs to be considered when evaluating the quadratic normalization integrals $\mathcal{I}_n$ defined in Equation (103). By combining Equations (93) and (103), we obtain

$$\mathcal{I}_n = \lim_{\epsilon \to 0} \frac{1}{R_g}\int_{R_{\rm S}}^{r_* - \epsilon} \omega(r)\,\varphi_n^2(r)\,dr + \frac{1}{R_g}\int_{r_* + \epsilon}^{\infty} \omega(r)\,\varphi_n^2(r)\,dr + R_g\left(\frac{v_- - v_+}{3\kappa_*}\right)\varphi_n^2(r_*), \tag{106}$$

which serves as the basis for computing the required normalization integrals.

5.6. Distribution Function for the Escaping Particles

Based on the solution for the Green's function, $f_{\rm G}$, which describes the relativistic particle distribution in the disk, we are also able to compute the Green's function distribution for the relativistic particles that escape from the disk to form the outflow. The number of particles escaping from the disk per unit energy per unit time is computed by performing a volume integration of the escape term $\dot{f}_{\rm esc}$ (Equation (29)) and also multiplying by the factor $4\pi E^2$ to convert the result to a number distribution (see Equation (3)). The result obtained is

$$\dot{N}_E^{\rm esc}(E) = 4\pi E^2 \int_{R_{\rm S}}^{\infty} 4\pi r\, H\, \dot{f}_{\rm esc}\, dr = (4\pi E)^2\, r_*\, H_*\, c\, A_0\, f_{\rm G}(E, r_*), \tag{107}$$

which is the Green's function number distribution for the escaping particles. The number of particles escaping from the disk per unit time with energy between E and $E + dE$ is equal to $\dot{N}_E^{\rm esc}\,dE$, and therefore the total number of particles escaping from the disk per unit time is given by the integral

$$\dot{N}_{\rm esc} = \int_{E_0}^{\infty} \dot{N}_E^{\rm esc}(E)\,dE \;\propto\; \mathrm{s}^{-1}. \tag{108}$$

We have set the lower bound of integration equal to the seed particle energy E_0 because there is no energy loss mechanism included in the model, and therefore all of the injected particles must continually gain energy until they escape from the disk. In similar fashion, the total energy carried away per unit time by the escaping particles is given by the integral

$$L_{\rm esc} = \int_{E_0}^{\infty} E\,\dot{N}_E^{\rm esc}(E)\,dE \;\propto\; \mathrm{erg\ s}^{-1}. \tag{109}$$

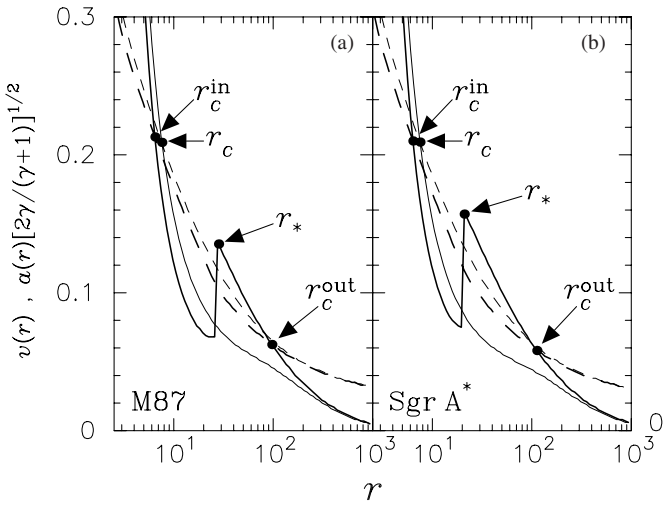

Figure 1. Accretion velocity v (solid lines) and isothermal sound speed a (dashed lines) plotted in units of c as functions of the radius r in units of $R_g \equiv GM/c^2$ for (a) M87 and (b) Sgr A*. The thick and thin lines denote the shocked and smooth solutions, respectively. The sound speed is multiplied by $[2\gamma/(\gamma+1)]^{1/2}$ so that the curves for v and a intersect at the critical points. The shock and critical point locations are indicated for each model using the notation discussed in the text.

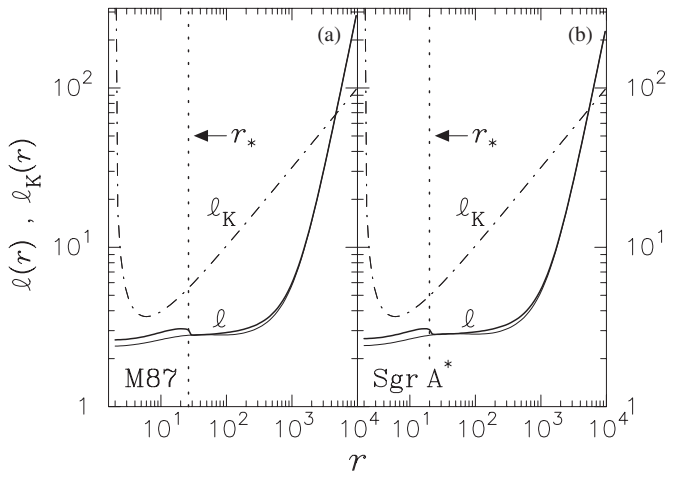

Figure 2. Specific angular momentum ℓ (solid lines) and Keplerian specific angular momentum $\ell_{\rm K}$ (dot-dashed lines) plotted in units of $R_g\, c$ as functions of the radius r in units of $R_g \equiv GM/c^2$ for (a) M87 and (b) Sgr A*. The thick and thin lines for ℓ denote the shocked and smooth solutions, respectively. The dotted vertical lines indicate the shock location for each model.

5.7. Evaluation of Solution Accuracy

It is important to have a separate means for evaluating the validity of the results obtained for the relativistic particle distribution using the power series solution for the Green's function given by Equation (98). Fortunately, there are several methods available that can be utilized for this purpose.

The first method is based on the conservation of particle number, which requires that the rate at which accelerated particles escape from the disk per unit time, $\dot{N}_{\rm esc}$, computed using Equation (108), must be equal to $4\pi r_* H_* A_0\, c\, n_*$ (see Equation (69)). The second method is based on the principle of global energy conservation, which requires that $L_{\rm esc}$ computed using Equation (109) is equal to $-\dot{M}\Delta\epsilon$ (see Equation (76)). This condition ensures that the power in the escaping particles is equal to the energy loss rate for the accretion flow at the shock location, hence eliminating any unphysical sources or sinks of energy.

In addition to the two global balance conditions described above, we can also test the solution for the Green's function $f_{\rm G}$ by calculating the associated number and energy density functions $n_r(r)$ and $U_r(r)$ using the Green's function integrals given by Equations (3). The results obtained for the number and energy densities in this way should agree closely with those computed via numerical integration of the fundamental differential equation (62), which leads to the formal solutions for $n_r = I_2$ and $U_r = I_3$ given by Equation (58). We will use these two methods to compute the number and energy densities in Section 6 in order to evaluate the robustness of the solution obtained for the Green's function.

6. ASTROPHYSICAL APPLICATIONS

In our numerical examples, the disk/outflow structures for M87 and Sgr A* are determined based on observational estimates for the black hole mass M, the mass accretion rate $\dot{M}$, and the jet kinetic power $L_{\rm jet}$. The multistep iterative procedure required to determine the dynamical structure for a particular source was summarized in Section 2.4, and the specific dynamical models we utilize for M87 and Sgr A* were discussed in detail by Das et al. (2009). These new dynamical solutions represent the first-ever self-consistent models for ADAF disks with isothermal shocks and a significant level of viscosity ($\alpha = 0.1$).

We briefly review the results obtained for the disk structure below, as part of our discussion of the new solutions for the Green's function describing the relativistic particle distribution in the disk/outflow system. In our numerical calculations, we utilize gravitational units for convenience unless otherwise noted. Hence we express the disk radius r and half-thickness H in units of $R_g \equiv GM/c^2$, the accretion velocity v and sound speed a in units of the speed of light c, the angular velocity Ω in units of c/R_g, the specific angular momentum ℓ in units of R_{gc}, and the energy transport rate per unit mass ϵ in units of c^2. In this convention, the Schwarzschild radius has the value $R_{\rm S} = 2$. Results for the relativistic particle number density n_r, energy density U_r, and Green's function $f_{\rm G}$ are presented in cgs units to facilitate comparison with previously published work. Following Narayan et al. (1997), we set $\gamma = 1.5$, which corresponds to an approximate equipartition between the gas and magnetic pressures.

6.1. M87

The application of the model to M87 is based on the observational values $M = 3.0 \times 10^9\, M_\odot$ (e.g., Ford et al. 1994), $\dot{M} = 1.34 \times 10^{-1}\, M_\odot\ {\rm yr}^{-1}$ (Reynolds et al. 1996), and $L_{\rm jet} = 5.5 \times 10^{43}\ {\rm erg\ s}^{-1}$ (Reynolds et al. 1996; Bicknell & Begelman 1996; Owen et al. 2000). The Shakura–Sunyaev viscosity parameter is set using $\alpha = 0.1$, which allows us to examine the performance of the model in the presence of a relatively high level of viscous dissipation.

The results obtained for the inflow speed $v(r)$ and the isothermal sound speed $a(r)$ in the shocked-disk model for M87 are plotted in Figure 1(a), and the corresponding radial distribution for the specific angular momentum $\ell(r)$ is compared with the Keplerian profile $\ell_{\rm K}(r)$ in Figure 2(a) (see Equation (4)). The dynamical parameters obtained for the M87 shocked-disk model are $\epsilon_- = 0.001516\, c^2$, $\epsilon_+ = \epsilon_0 = -0.005746\, c^2$, $\ell_0 = 2.6257\, R_g c$, $K_0 = 0.00608$, $r_* = 26.329\, R_g$, $r_c^{\rm in} = 6.462\, R_g$, and $r_c^{\rm out} = 96.798\, R_g$. The associated pre-shock and post-shock velocities and Mach numbers are $v_- = 0.138\, c$, $v_+ = 0.068\, c$, $\mathcal{M}_- = 1.427$, and $\mathcal{M}_+ = 0.701$, respectively, and for the disk

half-thickness at the shock location we obtain $H_* = 12.10\,R_g$. The value of ℓ merges with ℓ_K at $r_{edge} = 4658\,R_g$, which defines the outer edge of the ADAF region (Narayan et al. 1997).

The values for ϵ_+ and ϵ_- determine the energy budget for the jet via Equation (22), which states that $L_{jet} = -\dot{M}\Delta\epsilon$, where $\Delta\epsilon = \epsilon_+ - \epsilon_-$. In the case of M87, we obtain $L_{jet} = 0.0073\,\dot{M}\,c^2$, and therefore ∼0.7% of the incident accretion energy is used to power the jet outflow. This is close to the efficiency computed by Narayan & Fabian (2011) for this source, in their consideration of the accretion of slowly rotating matter onto a supermassive black hole. Adopting for the accretion rate $\dot{M} = 8.43 \times 10^{24}\,\mathrm{g\,s^{-1}}$ yields $L_{jet} \sim 5.5 \times 10^{43}\,\mathrm{erg\,s^{-1}}$, in agreement with the observed jet luminosity for M87. The results for the specific angular momentum ℓ plotted in Figure 2(a) are significantly sub-Keplerian, whether or not a shock is present, due to the relatively large value adopted for the viscosity parameter, $\alpha = 0.1$ (see Narayan et al. 1997). The evolution of the angular momentum distribution as the gas accretes is discussed in more detail in Section 7.

It is also interesting to compute the structure of an equivalent shock-free (smooth) disk model based on the same set of outer (incident) boundary conditions employed in the shocked-disk case. The comparison between the two models will help to illustrate the dynamical effect of the shock. In the smooth model for M87, we use the same value for the incident energy transport rate $\epsilon_- = 0.001516\,c^2$ and the outer radius $r_{edge} = 4658\,R_g$ as in the shocked case, and the resulting values for the accreted specific angular momentum and the accreted entropy parameter in the smooth model are $\ell_0 = 2.3988\,R_g c$ and $K_0 = 0.0084$, respectively. Since there is no shock present in this case, the specific energy transport rate is constant, and consequently $\epsilon_0 = \epsilon_+ = \epsilon_- = 0.001516\,c^2$. The smooth model possesses a single critical point, located at $r_c = 7.572\,R_g$, and its structure is consistent with results obtained by Narayan et al. (1997), who solved the identical set of ADAF conservation equations considered here, under the assumption of smooth flow. As demonstrated in Figure 1(a), the presence of the shock tends to reduce the sound speed, and therefore the temperature, due to the escape of energy from the disk into the outflow at the shock location. Hence, the gas in a shocked disk is more bound than in a smooth flow, a point that is discussed further in Section 7.

Once the dynamical structure of the disk/shock has been established, we can compute the Green's function describing the distribution of the relativistic particles in the disk using the procedure discussed in Section 5, which culminates in Equation (98). The results obtained for the particle transport parameters in the shocked-disk model are $B_0 = 0.01632$, $\dot{N}_0 = 2.75 \times 10^{46}\,\mathrm{s^{-1}}$, $\dot{N}_{esc} = 5.81 \times 10^{45}\,\mathrm{s^{-1}}$, and $A_0 = 0.0153$. The number and energy densities of the relativistic particles at the shock radius are $n_* = 1.62 \times 10^4\,\mathrm{cm^{-3}}$ and $U_* = 1.52 \times 10^2\,\mathrm{erg\,cm^{-3}}$, respectively. For comparison, the number density of the background (thermal) protons at the shock radius is $n_*^{th} = 2.08 \times 10^6\,\mathrm{cm^{-3}}$, and the corresponding energy density is $U_*^{th} = 5.86 \times 10^1\,\mathrm{erg\,cm^{-3}}$. We therefore conclude that $n_*/n_*^{th} \sim 0.0078$ and $U_*/U_*^{th} \sim 2.59$, and consequently the mean energy of the escaping particles, $\langle E\rangle = U_*/n_*$, is ∼333 times larger than the mean energy of the thermal protons at the shock radius, $\langle E_*^{th}\rangle = n_*^{th}/U_*^{th}$. The mass loss associated with the outflow is given by $\dot{M}_{out} = \dot{N}_{esc}\,m_p = 9.71 \times 10^{21}\,\mathrm{g\,s^{-1}}$, and consequently $\dot{M}_{out}/\dot{M} \sim 0.0012$, implying that the loss of mass from the disk into the outflow is completely negligible, as we have implicitly assumed by treating $\dot{M}$ as a global constant in our model.

Based on Equation (77), we find that $\langle E\rangle = 4.71\,E_0$, which confirms that the mean energy of the particles escaping to form the outflow is substantially higher than that of the seed particles injected with energy E_0. This ratio illustrates the cumulative effect of Fermi acceleration on the seed particles. The outwardly directed particle transport rate in the region $r > r_*$ is found to be $\dot{N}_I = 2.90 \times 10^{45}\,\mathrm{s^{-1}}$, and the inwardly directed particle transport rate for $r < r_*$ is $\dot{N}_{II} = -1.88 \times 10^{46}\,\mathrm{s^{-1}}$. We therefore find that ∼68% of the injected particles are ultimately advected across the event horizon and into the black hole, whereas ∼11% are able to diffuse outward through the disk to large radii, and ∼21% escape from the upper and lower surfaces of the disk to form the energetic outflow. We also note that the quantities $\dot{N}_0$, $\dot{N}_{esc}$, $\dot{N}_I$, and $\dot{N}_{II}$ satisfy Equation (70) as required.

In the shock-free (smooth) case, the particle transport parameters are $B_0 = 0.01632$, $\dot{N}_0 = 2.75 \times 10^{46}\,\mathrm{s^{-1}}$, $\dot{N}_{esc} = 0$, $A_0 = 0$, $n_* = 1.63 \times 10^4\,\mathrm{cm^{-3}}$, and $U_* = 4.97 \times 10^1\,\mathrm{erg\,cm^{-3}}$. Although there is no shock in this case, we leave the source located at $r = 26.329\,R_g$ for consistency. The corresponding number and energy density values for the thermal protons at the source radius are $n_*^{th} = 2.49 \times 10^6\,\mathrm{cm^{-3}}$ and $U_*^{th} = 8.88 \times 10^1\,\mathrm{erg\,cm^{-3}}$, respectively. In the smooth model, the outwardly directed particle transport rate is $\dot{N}_I = 2.13 \times 10^{45}\,\mathrm{s^{-1}}$, and the inwardly directed particle transport rate is $\dot{N}_{II} = -2.54 \times 10^{46}\,\mathrm{s^{-1}}$. Hence, only ∼8% of the particles diffuse outward through the disk to large radii and the remaining ∼92% are advected across the event horizon. The result obtained for the mean energy boost ratio at the source radius, $\langle E\rangle/E_0 = 1.53$, is significantly lower than that observed in the shocked-disk model because the only Fermi acceleration operative in the smooth disk is that due to the overall convergence of the accretion flow, which is much weaker than the concentrated acceleration obtained in the presence of the velocity discontinuity.

The computation of the solution for the Green's function includes the determination of the set of eigenvalues, λ_n, based on the derivative jump condition given by Equation (88). Since the eigenvalues form a sequence of increasingly positive numbers, it follows from Equation (98) that the first eigenvalue, λ_1, determines the shape of the particle distribution at high energies. The sequence of eigenvalues associated with the M87 particle transport model is plotted in Figure 3(a) for both shocked and smooth disks. The comparison between the two cases is interesting because the smooth disk only includes the acceleration associated with the overall convergence of the accretion flow, whereas the shocked model adds the concentrated acceleration occurring in the vicinity of the velocity discontinuity. In the shocked-disk case, we obtain for the first eigenvalue $\lambda_1 = 4.22$, and in the shock-free model we obtain $\lambda_1 = 4.90$. The hardening of the high-energy spectrum in the shocked disk clearly illustrates the dominance of shock acceleration over first-order Fermi compression in the background flow.

In Figure 4(a), we plot the Green's function energy distribution f_G for the accelerated particles in the M87 disk computed using Equation (98). Results are presented for both shocked and smooth disks. The presence of the shock results in a harder (flatter) energy spectrum at all radii as expected. The corresponding number and energy distributions for the escaping particles, $\dot{N}_E^{esc}$ and $E\dot{N}_E^{esc}$, respectively, are plotted in Figure 5(a) using Equation (107). At high energies, the escaping number distribution has a power-law shape, with $\dot{N}_E^{esc} \propto E^{-\alpha_*}$. Since the diffusion time for particles to escape from the disk is independent of the particle energy in our model (see Equation (29)), it follows that α_* is related to the first eigenvalue, λ_1, via $\alpha_* = \lambda_1 - 3$,

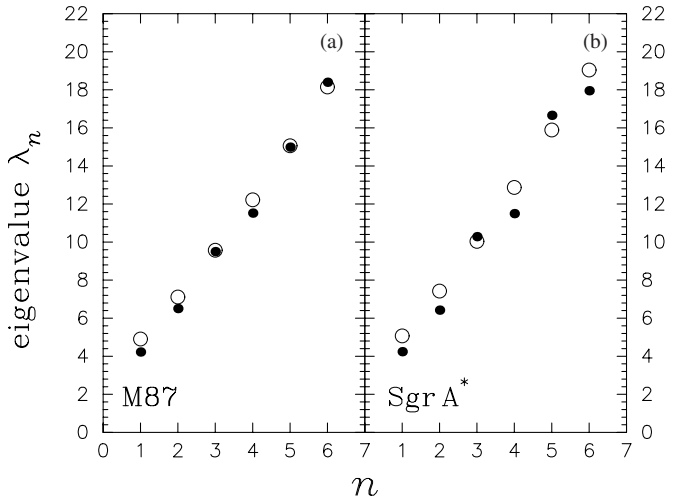

Figure 3. Eigenvalues λ_n plotted as a function of the index n for (a) M87 and (b) Sgr A*. Filled circles denote the shocked-disk model and open circles represent the results obtained in the corresponding smooth-disk model. Note the marked decrease in the first eigenvalue λ_1 when a shock is present, leading to characteristic spectral hardening.

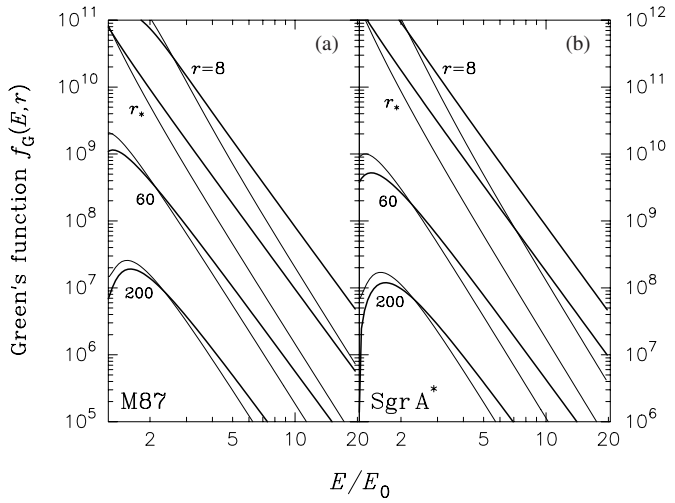

Figure 4. Green's function (Equation (98)) describing the distribution of particles in the disk plotted in units of erg^{-3} cm^{-3} as a function of energy E/E_0 and radius r in units of $R_g = GM/c^2$ for (a) M87 and (b) Sgr A*. The injection energy $E_0 = 0.002$ erg, corresponding to Lorentz factor $\Gamma_0 \equiv E_0/(m_p c^2) \approx 1.33$. The shocked and smooth solutions are denoted by the thick and thin lines, respectively. The enhanced Fermi acceleration due to the presence of the shock decreases the first eigenvalue λ_1 (see Figure 3), resulting in spectral hardening at high energies.

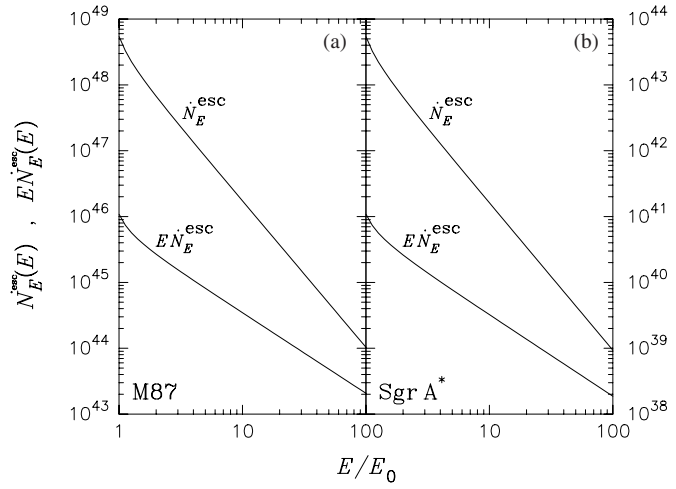

Figure 5. Number and energy distributions for particles escaping through the disk surfaces to form relativistic outflows in (a) M87 and (b) Sgr A*, plotted in cgs units using Equation (107). The total energy escape rate is consistent with estimates of the kinetic luminosity in the two sources.

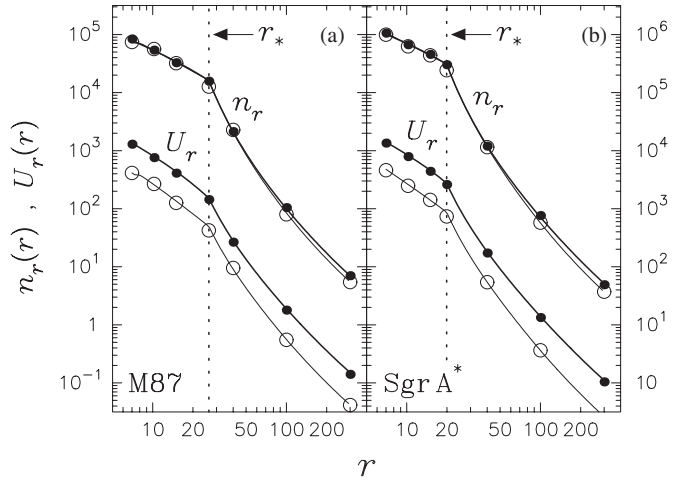

Figure 6. Relativistic particle number and energy densities, n_r and U_r, plotted in cgs units as functions of radius r in units of $R_g = GM/c^2$ for (a) M87 and (b) Sgr A*. Solid lines denote the density values computed using the formal solutions for the moments $I_2(r) = n_r(r)$ and $I_3(r) = U_r(r)$ given by Equation (58), and circles represent the values obtained using Equation (3) to numerically integrate the series solution for the Green's function (Equation (98)). Filled circles and thick lines represent the shocked-disk results; the corresponding smooth-disk results are denoted by the open circles and thin lines. The dotted vertical lines indicate the shock location for each model. The close agreement confirms the accuracy of the solution for the Green's function.

which yields $\alpha_* = 1.22$ in our model for M87. The flatness of the escaping particle energy spectrum is another reflection of the high efficiency of the particle acceleration process occurring in the shocked disk.

The total power in the escaping particles, computed using Equation (109), is found to be $L_{\rm esc} = 5.5 \times 10^{43}$ erg s^{-1}, which agrees with the value of $L_{\rm jet}$, as required for global energy conservation. This confirms that particle acceleration in the shocked, viscous disk is sufficient to power the observed outflows in M87. We can also check the value of the total particle escape rate $\dot{N}_{\rm esc}$ by computing it using the Green's function integration in Equation (108) and comparing the result with that obtained using the alternative formula given by Equation (69). Both methods yield the same result, $\dot{N}_{\rm esc} = 5.81 \times 10^{45}$ s^{-1}, which validates the solution obtained for the Green's function.

In Figure 6(a), we plot the relativistic particle number and energy density profiles, $n_r(r)$ and $U_r(r)$, respectively, computed by integrating the M87 Green's function $f_{\rm G}$ using Equations (3). Results are presented for both shocked and smooth disks. We can assess the accuracy of the Green's function solution by comparing the number and energy density values with those obtained using the formal solution for the nth moment $I_n(r)$ (Equation (58)), which is based on numerical integration of Equation (62). These results are also included in Figure 6(a). It is clear that the two methods agree quite closely, as they should, which confirms the accuracy of the series expansion for the Green's function given by Equation (98). The results obtained for the number density distribution in Figure 6(a) are very similar in the shocked and smooth disks, but the energy density values are amplified by a factor of ∼3 when a shock is present due to the enhanced level of particle acceleration.

6.2. Sgr A*

For Sgr A*, we adopt the values $M = 2.6 \times 10^6\, M_\odot$ (Schödel et al. 2002), $\dot{M} = 8.96 \times 10^{-7}\, M_\odot\ \mathrm{yr}^{-1}$ (Yuan et al. 2002; Quataert 2003), and $L_{\rm jet} = 5 \times 10^{38}\ \mathrm{erg\ s}^{-1}$ (Falcke & Biermann 1999). We also set $\gamma = 1.5$ and $\alpha = 0.1$. In Figure 1(b), we plot the profiles for the inflow speed $v(r)$ and the isothermal sound speed $a(r)$ obtained in both the shocked- and smooth-disk models for Sgr A*. In Figure 2(b), we plot the corresponding profiles for the specific angular momentum $\ell(r)$ and the Keplerian specific angular momentum $\ell_{\rm K}(r)$.

In the shocked-disk case, the results obtained for the model parameters are $\epsilon_- = 0.00134884\, c^2$, $\epsilon_+ = \epsilon_0 = -0.0085\, c^2$, $\ell_0 = 2.6728\, R_g c$, $K_0 = 0.005448$, $r_* = 19.917\, R_g$, $r_c^{\rm in} = 6.380\, R_g$, and $r_c^{\rm out} = 112.384\, R_g$. For the pre-shock and post-shock velocities and Mach numbers we find that $v_- = 0.159\, c$, $v_+ = 0.0748\, c$, $\mathcal{M}_- = 1.4578$, and $\mathcal{M}_+ = 0.6860$, respectively, and the disk half-thickness at the shock location is $H_* = 8.72\, R_g$. The source is located at $r_* = 19.917\, R_g$, and we find that $\ell = \ell_{\rm K}$ at radius $r_{\rm edge} = 5432\, R_g$, which is the outer edge of the ADAF region. In the case of Sgr A*, the energy-budget relation $L_{\rm jet} = -\dot{M}\Delta(\epsilon_+ - \epsilon_-)$ yields (cf. Equation (22)) $L_{\rm jet} = 0.0098\, \dot{M}\, c^2$, and therefore ∼1% of the incident accretion energy is converted into the kinetic energy of the outflowing jet particles. Utilizing the accretion rate $\dot{M} = 5.65 \times 10^{19}\ \mathrm{g\ s}^{-1}$ yields $L_{\rm jet} \sim 5.0 \times 10^{38}\ \mathrm{erg\ s}^{-1}$, which establishes that our shocked-disk dynamical model successfully accounts for the observed energetics of the accretion flow and the outflow in Sgr A*.

We can also obtain a smooth (shock-free) solution for the dynamical structure of Sgr A* by integrating the conservation equations using the same value for the incident energy transport rate ϵ_- as adopted in the shocked-disk model, but with no shock included. The value of ℓ_0 is then varied until we obtain $\ell = \ell_{\rm K}$ at the same outer radius, $r_{\rm edge} = 5432\, R_g$, as in the shocked disk. The resulting parameter values for the smooth solution are $\epsilon_0 = \epsilon_+ = \epsilon_- = 0.00134884\, c^2$, $\ell_0 = 2.416\, R_g c$, $K_0 = 0.008293$, and $r_c = 7.51135\, R_g$. These results are indicated in Figures 1(b) and 2(b). Note that once again we observe that the sound speed (and temperature) are significantly reduced when a shock is present.

The transport and acceleration of relativistic particles in the Sgr A* disk can be analyzed based on either the shocked or smooth dynamical profiles. The results obtained for the particle transport parameters in the shocked-disk model for Sgr A* are $B_0 = 0.021292$, $\dot{N}_0 = 2.5 \times 10^{41}\ \mathrm{s}^{-1}$, $\dot{N}_{\rm esc} = 5.63 \times 10^{40}\ \mathrm{s}^{-1}$, $A_0 = 0.01889$, $n_* = 3.09 \times 10^5\ \mathrm{cm}^{-3}$, $U_* = 2.74 \times 10^3\ \mathrm{erg\ cm}^{-3}$, and $\langle E\rangle/E_0 = 4.44$. For comparison, the corresponding values for the number and energy densities of the background (thermal) protons at the shock radius are $n_*^{\rm th} = 3.00 \times 10^7\ \mathrm{cm}^{-3}$ and $U_*^{\rm th} = 1.07 \times 10^3\ \mathrm{erg\ cm}^{-3}$, respectively. We therefore conclude that the mean energy of the escaping particles, $\langle E\rangle = U_*/n_*$, is ∼248 times larger than the mean energy of the thermal protons at the shock radius, $\langle E_*^{\rm th}\rangle = n_*^{\rm th}/U_*^{\rm th}$. The mass loss rate into the outflow is $\dot{M}_{\rm out} = \dot{N}_{\rm esc}\, m_p = 9.40 \times 10^{16}\ \mathrm{g\ s}^{-1}$, and consequently $\dot{M}_{\rm out}/\dot{M} \sim 0.0017$, confirming that the loss of mass from the disk into the outflow is negligible, as we have assumed.

In the shock-free (smooth) case, the transport parameters are given by $B_0 = 0.021292$, $\dot{N}_0 = 2.5 \times 10^{41}\ \mathrm{s}^{-1}$, $\dot{N}_{\rm esc} = 0$, $A_0 = 0$, $n_* = 3.10 \times 10^5\ \mathrm{cm}^{-3}$, $U_* = 8.74 \times 10^2\ \mathrm{erg\ cm}^{-3}$, and $\langle E\rangle/E_0 = 1.41$. The source is located at $r = 19.917\, R_g$ to facilitate comparison with the shocked case. The corresponding number and energy density values for the thermal protons at the source radius are $n_*^{\rm th} = 3.56 \times 10^7\ \mathrm{cm}^{-3}$ and $U_*^{\rm th} = 1.65 \times 10^3\ \mathrm{erg\ cm}^{-3}$, respectively. Once again we note that the mean energy boost ratio at the source location, $\langle E\rangle/E_0$, is significantly greater when a shock is present, which reflects the dominance of the Fermi acceleration occurring near the velocity discontinuity.

In the shocked-disk model for Sgr A*, the outwardly directed particle transport rate for $r > r_*$ is $\dot{N}_{\rm I} = 2.38 \times 10^{40}\ \mathrm{s}^{-1}$, and the inwardly directed transport rate for $r < r_*$ is $\dot{N}_{\rm II} = -1.70 \times 10^{41}\ \mathrm{s}^{-1}$. Hence, ∼68% of the test particles are advected across the horizon, ∼10% diffuse outward to large radii, and ∼22% escape through the disk surfaces to power the outflows. Conversely, in the smooth-disk model, we find that the outwardly directed transport rate is $\dot{N}_{\rm I} = 1.56 \times 10^{40}\ \mathrm{s}^{-1}$ and the inwardly directed transport rate is $\dot{N}_{\rm II} = -2.34 \times 10^{41}\ \mathrm{s}^{-1}$, indicating that ∼94% of the particles are advected into the black hole and only ∼6% are able to diffuse to large radii.

The sequence of eigenvalues obtained in the Sgr A* application is plotted in Figure 3(b). The eigenvalues form a sequence of increasingly positive real numbers, and therefore the first eigenvalue, λ_1, determines the shape of the Green's function particle distribution at high energies. In the shocked-disk case, we obtain $\lambda_1 = 4.24$, and in the shock-free model we find that $\lambda_1 = 5.07$. Comparison between the shocked- and smooth-disk cases reveals the characteristic spectral hardening at high energies due to the efficiency of the shock acceleration process.

The Green's function for the accelerated relativistic particles in the Sgr A* disk can be computed using Equation (98) based on either the shocked or smooth dynamical structures. The results obtained are plotted in Figure 4(b). As expected, the shocked-disk model produces a much harder energy spectrum due to the enhanced Fermi acceleration occurring near the velocity discontinuity. The associated number and energy distributions $\dot{N}_E^{\rm esc}$ and $E\dot{N}_E^{\rm esc}$ for the escaping particles are computed using Equation (107) and plotted in Figure 5(b). The escaping number distribution has a power-law shape at high energies, with $\dot{N}_E^{\rm esc} \propto E^{-\alpha_*}$, where $\alpha_* = \lambda_1 - 3$. In our model for Sgr A* we obtain $\alpha_* = 1.24$.

By utilizing Equation (109), we find that the total power in the escaping particles is $L_{\rm esc} = 5 \times 10^{38}\ \mathrm{erg\ s}^{-1}$, which is consistent with the observational value of $L_{\rm jet}$, hence confirming that the shock acceleration model developed here is capable of powering the observed outflows in Sgr A*. As a further check on the normalization of the escaping particle spectrum, we can compute the total particle escape rate $\dot{N}_{\rm esc}$ using Equations (69) and (108). Both equations yield the same result, $\dot{N}_{\rm esc} = 5.63 \times 10^{40}\ \mathrm{s}^{-1}$, as required, which establishes that the Green's function is properly normalized.

In Figure 6(b), we compare the results for the Sgr A* relativistic particle number and energy densities $n_r(r) = I_2(r)$ and $U_r(r) = I_3(r)$ computed using the Green's function integrals (Equations (3)) with the corresponding profiles computed using the formal solution for the nth moment $I_n(r)$ given by Equation (58), which is based on numerical integration of Equation (62). The two sets of results are consistent, which establishes the validity of the Green's function series expansion given by Equation (98). The number density curves plotted in Figure 6(b) for the shocked- and smooth-disk models are very similar, but the energy density curve is boosted by a factor of ∼3 in the shocked disk, reflecting the enhanced particle acceleration created by the velocity discontinuity.

7. DISCUSSION AND CONCLUSION

In this paper, we have presented a rigorous analytical model for the production of energetic particles via diffusive shock acceleration in advection-dominated accretion disks. Such disks are ideal sights for first-order Fermi acceleration because the plasma is tenuous and the gas is collisionless, and therefore a small population of particles can gain a great deal of energy via repeated shock crossings. The main result obtained here is a detailed description of the Green's function describing the energy/space distribution of the accelerated particles in the disk (Equation (98)). The solution for the Green's function is also used to compute the energy distribution of the particles escaping from the disk to form the energetic outflow.

It has been recognized for some time that advection-dominated disks have a positive Bernoulli parameter, which implies that the gas is unbound from the black hole (see Narayan et al. 1997; Blandford & Begelman 1999). In this sense, the original ADAF model is not fully self-consistent. Despite this problem, no microphysical mechanism for funneling the excess gravitational binding energy into a population of outflowing particles has been identified in the previous literature. In this paper, we have investigated the possibility that diffusive shock acceleration in viscous disks serves as the primary mechanism for transferring the excess gravitational binding energy to a population of escaping energetic particles. Diffusive shock acceleration is quite efficient in the tenuous gas around underfed black holes, but the process only results in bulk heating in more luminous X-ray sources in which the gas is too dense to allow efficient Fermi acceleration of a small population of relativistic particles. This interpretation is consistent with the observed anticorrelation between radio/outflow strength and X-ray luminosity (Reynolds et al. 1996). Our results suggest that the efficiency of the diffusive shock acceleration mechanism is high enough to explain the observed outflows, while at the same time solving the long-standing problem of the stability of ADAF disks.

We have developed detailed models for the particle populations in the accretion disks around the central black holes in Sgr A* and M87 and we conclude that the observed jet power in the outflows from these sources can be provided via shock acceleration. The associated Green's function solutions are plotted in Figure 4, and the escaping particle distributions are plotted in Figure 5. The validity of the Green's function describing the particle distribution in each source was confirmed via independent calculations of the total particle number and energy density distributions in the disk (see Figure 6). By comparing the results obtained in shocked and smooth disks satisfying the same outer boundary conditions, we have clearly demonstrated the crucial role of the shock in creating a very hard high-energy distribution versus the weaker form of acceleration associated with the general convergence of the background accretion flow. We find that the presence of a shock is required in order to create a population of particles that can diffuse out of the disk to form the observed outflows; the acceleration associated with the general convergence of the background accretion flow is not adequate.

The terminal (asymptotic) Lorentz factor, Γ_∞, of the jet emanating from the disk can be computed using the relation $\Gamma_\infty = \langle E\rangle/(m_p c^2)$. For M87 and Sgr A*, we obtain in the case of a proton outflow $\Gamma_\infty = 6.26$ and $\Gamma_\infty = 5.91$, respectively. The associated values for the mean energy boost ratio are given by $\langle E\rangle/E_0 = 4.71$ and $\langle E\rangle/E_0 = 4.44$ for M87 and Sgr A*, respectively. We find that in the corresponding shock-free models, the energy is boosted by a factor of only ~1.4–1.5. This clearly establishes the essential role of the shock in efficiently accelerating particles up to very high energies, well above the energy required to escape from the vicinity of the black hole.

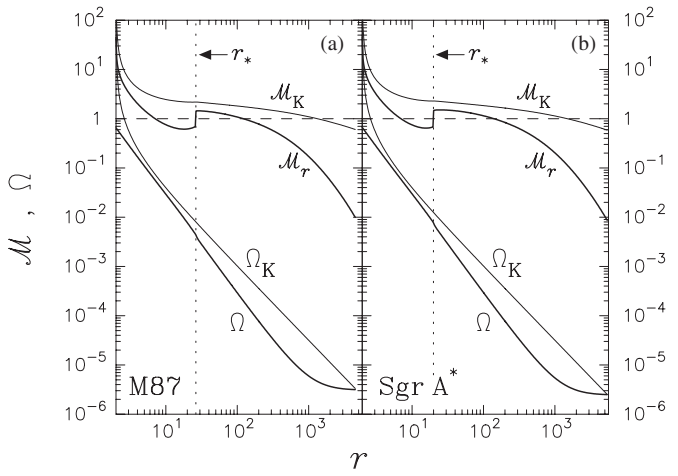

Figure 7. Angular velocity Ω and corresponding Keplerian value Ω_K plotted in units of c/R_g as functions of radius r in units of $R_g = GM/c^2$ for (a) M87 and (b) Sgr A*. The radial Mach number $\mathcal{M}_r$ and the Keplerian orbital Mach number $\mathcal{M}_K$ are also indicated. The dotted vertical lines indicate the shock location for each model. See the discussion in the text.

7.1. Angular Momentum Variation

The dynamical model employed here was fully described by Das et al. (2009) and is based on the standard set of ADAF conservation equations considered by Narayan et al. (1997). The conservation equations are supplemented by the inner boundary conditions developed by Becker & Le (2003) which allow the calculation of starting values for the physical variables close to the horizon. The fundamental model parameters are the specific energy of the gas supplied at a large radius ϵ_-, the Shakura–Sunyaev viscosity parameter α, and the ratio of specific heats γ. The formation of a shock requires that the flow possess at least two critical points. This possibility has been studied by many authors (e.g., Abramowicz & Zurek 1981; Chakrabarti 1989a, 1989b, 1990, 1996). Flows with discontinuities must first pass through an outer critical point, and subsequently through an isothermal shock and an inner critical point in order to represent physically acceptable accretion solutions.

For a given set of input parameters ϵ_-, α, and γ, the computational procedure outlined in Section 3 produces unique values for the accreted specific energy ϵ_0, the accreted specific angular momentum ℓ_0, the horizon entropy parameter K_0, the shock radius r_*, the inner critical point radius $r_c^{\rm in}$, and the outer critical point radius $r_c^{\rm out}$. As expected, the outer critical radius, $r_c^{\rm out}$, is comparable to the Bondi radius, at which the thermal energy of the accreting gas equals the gravitational potential energy.

The results for the specific angular momentum plotted in Figure 2 exhibit a sharp drop close to the outer edge, $r \sim r_{\rm edge}$. This phenomenon is explored in more detail in Figure 7, where we compare the angular velocity distribution $\Omega(r)$ with the Keplerian profile $\Omega_K(r)$ (Equation (4)). At the outer edge of the disk, $\Omega = \Omega_K$, but the orbital motion soon becomes significantly sub-Keplerian due to the strong viscous drag between adjacent annuli in the disk, which tends to lock them together, leading to solid-body rotation with $\Omega(r) \sim$ constant. The initial drop in $\ell(r)$ observed in Figure 2 reflects the approximately rigid rotation at large radii. This behavior is consistent with the results

obtained by Narayan et al. (1997) in their study of viscous ADAF disks. The same behavior was also observed more recently by Narayan & Fabian (2011) in their study of the Bondi accretion of slowly rotating matter onto supermassive black holes.

To understand this phenomenon quantitatively, we rewrite Equation (7) in the equivalent form

$$\frac{d\ln\Omega}{d\ln r} = \frac{\mathcal{M}_r\,\mathcal{M}_{\rm K}}{\alpha}\left(\frac{\ell_0}{\ell}-1\right). \tag{110}$$

where

$$\mathcal{M}_r \equiv \frac{v}{a}, \qquad \mathcal{M}_{\rm K} \equiv \frac{r\Omega_{\rm K}}{a} \tag{111}$$

denote the Mach numbers for the radial flow velocity and the Keplerian orbital velocity, respectively. In the outer region, close to $r \sim r_{\rm edge}$, we note that $\ell \gg \ell_0$ (see Figure 2), and therefore Equation (110) reduces to

$$\frac{d\ln\Omega}{d\ln r} \sim -\frac{\mathcal{M}_r\,\mathcal{M}_{\rm K}}{\alpha}, \qquad r \sim r_{\rm edge}. \tag{112}$$

The Mach numbers $\mathcal{M}_r$ and $\mathcal{M}_{\rm K}$ are plotted in Figure 7. The radial flow in the outer region is highly subsonic, i.e., $\mathcal{M}_r \ll 1$, whereas $\mathcal{M}_{\rm K} \sim 1$ for the azimuthal Keplerian flow. This leads to strong viscous coupling, and the associated viscous timescale is therefore much shorter than the characteristic accretion timescale at that radius. This effect explains the near-constancy of Ω in the outer region. The subsequent inward acceleration of the flow causes the radial Mach number to increase, which drives up the value of $|d\ln\Omega/d\ln r|$, resulting in the differential rotation seen in Figure 7. In the inner region, the specific angular momentum ℓ nearly levels off (see Figure 2), exhibiting a gradual decline as $r \to R_{\rm S}$ due to the dwindling viscous stress, which vanishes at the horizon since no stress can be supported there (Weinberg 1972).

The general trend of decreasing ℓ is temporarily reversed near the shock, where ℓ actually increases slightly due to the fact that the particles are moving from a supersonic region with low pressure and weak viscous coupling to a subsonic region with higher pressure and strong viscous coupling. In this situation, the particles near the shock gain more angular momentum from the downstream (subsonic) gas than they lose to the upstream (supersonic) gas. The imbalance between these two effects causes the particles to gain angular momentum as they pass through the vicinity of the shock. In the post-shock region, the angular momentum ℓ resumes its gradual decrease to the horizon value ℓ_0, which represents the specific angular momentum of the particles entering the black hole.

7.2. Comparison with Cosmic-Ray Acceleration

The model presented here parallels the earliest developments in the study of the diffusive acceleration of cosmic rays at supernova-driven shock waves. The transport equation we use (Equation (24)) is essentially the same one introduced by Blandford & Ostriker (1978), although the velocity profile and the location of the shock in an accretion disk are new features. However, the basic principle is the same. In the cosmic-ray application, the particle acceleration is powered by the supernova explosion, whereas in the accretion disk application, the acceleration is powered by the release of gravitational binding energy. Either mechanism provides copious energy for the shock, which efficiently transfers it to a population of high-energy particles via the first-order Fermi process.

It is therefore interesting to compare the first eigenvalue obtained in the shocked-disk model with the value computed using the classic plane-parallel model for cosmic-ray acceleration in supernova-driven shock waves. In the cosmic-ray application, the Green's function has a power-law shape with index (e.g., Blandford & Ostriker 1978)

$$\lambda_{\rm CR} = \frac{3\,R}{R-1}, \qquad R = \frac{v_-}{v_+}, \tag{113}$$

where R is the shock compression ratio. In the shocked-disk model, the compression ratio R is computed using the isothermal shock jump condition given by Equation (23). Based on the M87 parameters, we find that $R = 2.04$, which yields $\lambda_{\rm CR} = 5.90$. This is significantly larger than the value $\lambda_1 = 4.22$ obtained in the shocked-disk model for M87, and therefore we reach the surprising conclusion that the particle spectrum in the disk is much harder than would be obtained in the cosmic-ray application for a shock with the same compression ratio. In the case of Sgr A*, we obtain for the compression ratio $R = 2.13$, and consequently Equation (113) yields for the equivalent supernova-driven shock $\lambda_{\rm CR} = 5.67$. As in the case of M87, we note that the first eigenvalue in the Sgr A* application, $\lambda_1 = 4.24$, is much less than $\lambda_{\rm CR}$. *These results suggest that the presence of the disk environment surrounding the shock has a profound influence on the acceleration of the particles.*

We can gain further insight into this issue by comparing the mean energy of the accelerated particles, $\langle E\rangle$, at the shock location in both the disk and cosmic-ray scenarios. The mean energy in the cosmic-ray application is given by (Blandford & Ostriker 1978)

$$\langle E\rangle_{\rm CR} = \frac{3}{4-R}\,E_0, \tag{114}$$

where E_0 is the energy of the injected seed particles. Using the shock compression ratio $R = 2.04$ obtained in the M87 case yields $\langle E\rangle_{\rm CR}/E_0 = 1.53$ for the equivalent cosmic-ray shock. This is much less than the corresponding result $\langle E\rangle/E_0 = 4.71$ obtained in the M87 shocked-disk model. In the Sgr A* application, we have $R = 2.13$ and consequently $\langle E\rangle_{\rm CR}/E_0 = 1.60$ for the equivalent cosmic-ray shock. Once again, this is much less than the value $\langle E\rangle/E_0 = 4.44$ obtained in the shocked-disk model for Sgr A*. Since the shock compression ratio is the same in each of these comparisons, the dramatic difference between the two results must be due to the different environments surrounding the shock in the two situations.

In the model explored here, the shock is embedded in an accretion flow which makes an additional contribution to the particle acceleration due to the overall convergence of the background plasma. This additional component of acceleration is not included in the plane-parallel models for cosmic-ray acceleration in supernova-driven shock waves. However, the additional acceleration due to the background flow convergence is actually quite weak, and therefore this effect is not likely to explain the strong enhancement in the energy boost ratio $\langle E\rangle/E_0$ when comparing a supernova-driven shock to an accretion-driven shock of the same compression ratio.

We believe that the marked increase in efficiency in the disk case versus the cosmic-ray shock model stems from the nature of the particle transport in the region surrounding the shock. In the plane-parallel cosmic-ray shock, the upstream and downstream flows have constant velocity and density, and the region upstream from the shock has no net particle flux,

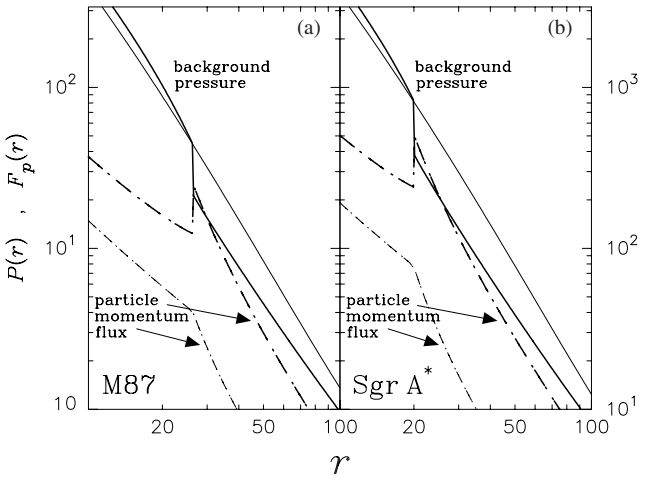

Figure 8. Background pressure P (solid lines) and relativistic particle vertical momentum flux F_p (Equation (115), dot-dashed lines) plotted in cgs units as functions of radius r in units of $R_g = GM/c^2$ for (a) M87 and (b) Sgr A*. Thick and thin lines denote shocked- and smooth-disk solutions, respectively. Particles are expected to escape when the momentum flux exceeds the background pressure, which occurs near the shock, if one is present. If no shock is present, $P \gg F_p$, and the particles are confined to the disk.

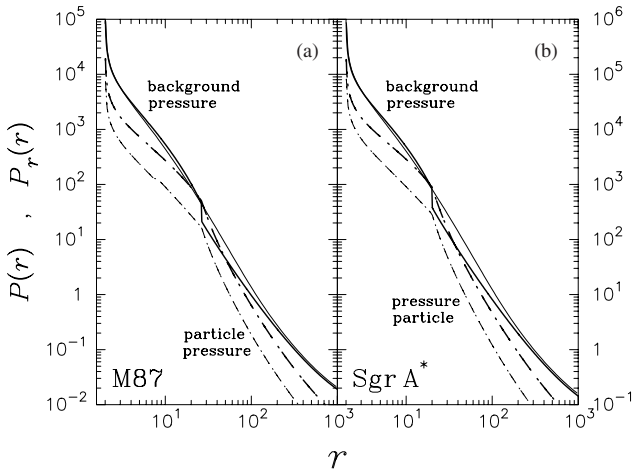

Figure 9. Background pressure P (solid lines) and relativistic particle pressure $P_r = U_r/3$ (dot-dashed lines) plotted in cgs units as functions of radius r in units of $R_g = GM/c^2$ for (a) M87 and (b) Sgr A*. Thick lines denote the shocked-disk solution, and thin lines represent the corresponding smooth-disk results. When a shock is present, the relativistic particle pressure slightly exceeds the background pressure near the shock. When no shock is present, the particle pressure is insignificant.

assuming the particle source is located at the shock. In this situation, all of the particles are ultimately swept away by advection into the downstream region. On the other hand, in the accretion disk context, the number density of the scattering centers increases strongly toward the event horizon, and this profoundly alters the nature of the particle transport upstream and downstream from the shock. We find that ∼10% of the particles in the disk are able to diffuse back across the shock into the far upstream region, to be "recycled" across the shock many more times than occurs in the plane-parallel cosmic-ray shock. The mean fractional energy increase generated by each shock crossing is $\sim|\Delta v/c|$, and therefore the energy of the relativistic particles in the disk can grow to values far exceeding what would be possible in the classic model for diffusive cosmic-ray acceleration, even though the shock compression ratio is the same in both cases.

7.3. Spatial Distribution of Escaping Particles

We have assumed here that all of the escaping relativistic particles emanate only from the shock location. This is expected to be the case since the shock acts as the epicenter of the acceleration process that powers the escaping particles. We can examine the validity of this assumption by analyzing the detailed results we have obtained for the particle distribution in the disk. In particular, it is interesting to compare the momentum flux of the diffusing particles with confining pressure provided by the background gas and the magnetic field. The vertical momentum flux of the diffusing particles is given by

$$F_p = \frac{U_r}{c}\, v_{\rm diff}, \qquad v_{\rm diff} = \frac{3\kappa}{H}, \tag{115}$$

where $v_{\rm diff}$ denotes the vertical diffusion velocity, and the spatial diffusion coefficient κ is evaluated using Equation (32). The vertical momentum flux F_p is compared with the background pressure P for the M87 and Sgr A* models in Figure 8. Note that in the smooth-disk models, the background pressure greatly exceeds the vertical momentum flux throughout the disk. However, when a shock is present, there is a small region around the shock where $F_p > P$ and the particles are expected to escape. This supports our assumption that particle escape is strongly focused at the shock location.

7.4. Test-particle Approximation

In the present work, we have utilized the "test-particle" hypothesis, in which the dynamical effect of the pressure of the accelerated particles is neglected. However, the marked flatness of the particle energy distribution in the shocked-disk application suggests that the particle pressure may be significant, and therefore it is important to compare the pressure of the relativistic particles with that of the background, composed of the thermal gas and the magnetic field, which are assumed to be in equipartition. If the pressure of the accelerated particles becomes comparable to or exceeds the background pressure, as occurred in the earliest models for supernova-driven cosmic-ray acceleration, then clearly the test-particle approximation would have to be abandoned and it would be necessary to include the pressure of the accelerated particles in the dynamical model in order to ensure complete self-consistency. In the context of cosmic-ray acceleration, this led to the development of the "two-fluid" model (e.g., Becker & Kazanas 2001).

In Figure 9, we compare the background pressure P with the pressure of the accelerated relativistic particles, $P_r = U_r/3$, computed by integrating the Green's function expansion using Equation (3). We find that in the smooth (shock-free) disk, the relativistic particle pressure is never dynamically important. In the shocked disk, P exceeds P_r everywhere except in the immediate vicinity of the shock, where they are comparable. This suggests that, as was found in the early models of cosmic-ray acceleration, the pressure of the accelerated particles is likely to alter the dynamical structure of the flow, and it may lead to a "softened" shock transition, possibly containing a discontinuous "subshock" (e.g., Becker & Kazanas 2001). The inclusion of the dynamical effect of the relativistic particle pressure is beyond the scope of the present paper, but it will be the subject of future investigation. However, since the particle pressure barely exceeds that of the background, even at the shock location, we do not expect substantial alteration of the disk structure compared with the results presented here.

7.5. Conclusion

Our results establish that the kinetic power in the outflows around M87 and Sgr A* can be explained as a consequence of accretion-driven, diffusive particle acceleration in viscous, shocked accretion disks. In applications to M87 and Sgr A*, we find that the energy of the relativistic particles that escape to form the outflow exceeds that of the thermal background gas at the shock radius by a factor of ∼300. The resulting kinetic power in the jet is $\sim 0.01\,\dot{M}c^2$. The shock efficiently channels gravitational binding energy into a small population of escaping particles, thereby explaining the formation of the observed outflows around radio-loud black holes, and also resolving the long-standing problem of the stability of ADAF disks. In fact, it can be argued that the self-consistency of the ADAF model *requires* the presence of a shock since it is the only identified microphysical mechanism capable of converting the excess gravitational binding energy into particle energy, thereby stabilizing the disk and allowing the remaining gas to accrete. We therefore conclude that a standing accretion shock may be an essential ingredient in understanding many observed disk/outflow systems.

The authors are grateful to the anonymous referee for providing several interesting comments that led to substantial improvements in the manuscript.

REFERENCES

Abramowicz, M. A., & Chakrabarti, S. K. 1990, ApJ, 350, 281
Abramowicz, M. A., & Zurek, W. H. 1981, ApJ, 246, 314
Becker, P. A., Das, S., & Le, T. 2008, ApJ, 677, L93
Becker, P. A., & Kazanas, D. 2001, ApJ, 546, 429
Becker, P. A., & Le, T. 2003, ApJ, 588, 408
Bicknell, G. V., & Begelman, M. C. 1996, ApJ, 467, 597
Blandford, R. D., & Begelman, M. C. 1999, MNRAS, 303, L1
Blandford, R. D., & Ostriker, J. P. 1978, ApJ, 221, L29
Chakrabarti, S. K. 1989a, PASJ, 41, 1145
Chakrabarti, S. K. 1989b, ApJ, 347, 365
Chakrabarti, S. K. 1990, Theory of Transonic Astrophysical Flows (Singapore: World Scientific Publishing)
Chakrabarti, S. K. 1996, ApJ, 464, 664
Chakrabarti, S. K., & Das, S. 2004, MNRAS, 349, 649
Das, S., Becker, P. A., & Le, T. 2009, ApJ, 702, 649
Das, S., Chattopadhyay, I., & Chakrabarti, S. K. 2001, ApJ, 557, 983
De Villers, J.-P., Hawley, J. F., & Krolik, J. H. 2003, ApJ, 599, 1238
Falcke, H., & Biermann, P. L. 1999, A&A, 342, 49
Fermi, E. 1954, ApJ, 119, 1
Ford, H. C., Harms, R. J., Tsvetanov, Z. I., et al. 1994, ApJ, 435, L27
Frank, J., King, A. R., & Raine, D. J. 2002, Accretion Power in Astrophysics (Cambridge: Cambridge Univ. Press)
Jones, F. C., & Ellison, D. C. 1991, Space Sci. Rev., 58, 259
Le, T., & Becker, P. A. 2004, ApJ, 617, L25
Le, T., & Becker, P. A. 2005, ApJ, 632, 476
Le, T., & Becker, P. A. 2007, ApJ, 661, 416
Lu, J., Gu, W., & Yuan, F. 1999, ApJ, 523, 340
Narayan, R., & Fabian, A. C. 2011, MNRAS, 415, 3721
Narayan, R., Kato, S., & Honma, F. 1997, ApJ, 476, 49
Owen, F. N., Eilek, J. A., & Kassim, N. E. 2000, ApJ, 543, 611
Paczyński, B., & Wiita, P. J. 1980, A&A, 88, 23
Quataert, E. 2003, Astron. Nachr., 324, 435
Reynolds, C. S., Matteo, T. D., Fabian, A. C., Hwang, U., & Canizares, C. R. 1996, MNRAS, 283, L111
Schödel, R., Ott, T., Genzel, R., et al. 2002, Nature, 419, 694
Shakura, N. I., & Sunyaev, R. A. 1973, A&A, 24, 337
Yang, R., & Kafatos, M. 1995, A&A, 295, 238
Yuan, F., Markoff, S., & Falcke, H. 2002, A&A, 383, 854
Weinberg, S. 1972, Gravitation and Cosmology (New York: Wiley)